Aki Haapaniemi

Simulation of Acoustic Wall Reflections Using the Finite-Difference Time-Domain Method

School of Electrical Engineering

Thesis submitted for examination for the degree of Master of Science in Technology.

Espoo 24.8.2012

Thesis supervisor:

Assoc. Professor Tapio Lokki

Thesis instructor:

Alex Southern, Ph.D.

A? **Aalto University**
School of Electrical
Engineering

Author: Aki Haapaniemi

Title: Simulation of Acoustic Wall Reflections Using the Finite-Difference Time-Domain Method

Date: 24.8.2012   Language: English   Number of pages:8+66

Department of Signal Processing and Acoustics

Professorship: Acoustics and Audio Signal Processing   Code: S-89

Supervisor: Assoc. Professor Tapio Lokki

Instructor: Alex Southern, Ph.D.

In this thesis, the reflection characteristics of layered wall structures are studied using the standard rectilinear (SRL) finite-difference time-domain (FDTD) method for modelling sound wave propagation. The structures consist of a panel with slats combined with a back wall, forming a cavity in between. Outwardly similar structures are known to have resonant properties and are generally known as *resonant absorbers* or *distributed Helmholtz resonators*. The structures studied in this thesis, however, are in a different parameter range and do not include absorptive material. They are found in practical use in, e.g., the Helsinki Music Centre Concert Hall. The various features of the structure are varied to establish how the reflection responses change with the features.

The relevant backgound in acoustics – including wave phenomena, measurement methods and acoustic modelling methods – is briefly reviewed. The basics of the SRL FDTD method is introduced in the context of the 3-D method. Introductory simulations are done to explore the nature of the 2-D and 3-D methods, and issues regarding the simulation setup are addressed. A comparison case of the 2-D and 3-D methods shows that the results can be qualitatively equivalent for structures having one axis of symmetry. The 2-D method is deemed a better suited choice for the work in this thesis.

The investigation was conducted through frequency- and time-domain analysis, diffusion measurements and visualizations. The studied structures were found to exhibit various degrees of comb filtering effects and frequency-dependent spatial and temporal spreading.

Keywords: FDTD, room acoustics, sound reflection, wave propagation visualization, diffusion measurement

Tekijä: Aki Haapaniemi

Työn nimi: Seinärakenteiden akustisten heijastusten simulointi FDTD-menetelmällä

Tässä diplomityössä tutkitaan kerrosteisten seinärakenteiden akustisia ominaisuuksia simuloimalla ääniaallon etenemistä SRL FDTD -menetelmällä. Tutkittavat rakenteet koostuvat säleisestä paneelista ja takaseinästä, joiden väliin muodostuu ilmatila. Ulkoisesti samankaltaiset rakenteet tunnetaan alan kirjallisuudessa yleisesti resonoivina vaimentimina. Tässä opinnäytetyössä tutkitut rakenteet ovat kuitenkin mitoiltaan eri luokassa, eivätkä sisällä vaimentavaa materiaalia. Rakenteita löytyy esim. Helsingin Musiikkitalon konserttisalista.

Aiheen kannalta olennainen taustatieto, liittyen ääniaallon ominaisuuksiin, mittausmenetelmiin ja mallinnusmenetelmiin, käsitellään lyhyesti. SRL FDTD -simulaatiomenetelmän perusteet esitellään 3-D menetelmän muodossa. Alustavat simulaatiot toimivat johdantona 2-D ja 3-D menetelmien ominaisuuksiin ja lisäksi käsitellään simulaatioiden toteutukseen liittyviä asioita. 2-D ja 3-D menetelmiä vertaileva tapaus osoittaa, että saatavat tulokset ovat laadullisesti vastaavia, kun tutkittavassa rakenteessa on yksi symmetria-akseli ja toteutukset vastaavat toisiaan. Näin 2-D menetelmä osoittautuu sopivammaksi tätä opinnäytetyötä varten.

Tutkimus toteutettiin taajuus- ja aika-tason analyysillä, diffuusiomittauksilla ja visualisaatioilla. Rakenteiden todettiin aiheuttavan kampasuodatusta sekä taajuudesta riippuvaa äänienergian paikallista ja ajallista leviämistä.

Preface

The work for this thesis was done as a research assistant within the Virtual Acoustics research team at the Department of Media Technology in Aalto University School of Science, during January–August 2012. I would like to express my gratitude to the Professors Tapio Lokki and Lauri Savioja for giving me the opportunity to work on this thesis project in their team and for their ongoing encouragement and help along the way.

I am grateful to my instructor Ph.D. Alex Southern for copious amounts of valuable advice, encouraging feedback and helpful discussions. He always found the time to help me regardless of his own busy schedule. I would also like to thank the whole Virtual Acoustics research team (including the summer trainees) and the personnel of the Department of Media Technology for contributing to a very pleasant working environment. It has been a pleasure to work amidst such a nice bunch of people. Last but not least, I am grateful to my parents, brothers and friends for being there and believing in me, even when I did not feel like doing so myself.

Otaniemi, 24.8.2012

Aki Haapaniemi

Contents

Symbols and abbreviations

Symbols

c	speed of sound
p	acoustic pressure
t	time
v	particle velocity
ρ_0	density of air
ω	angular velocity
k	wavenumber
f	frequency
Q	volume velocity
R	complex reflection coefficient
φ	phase
α	absorption coefficient
Z_w	wall impedance
ξ_w	specific wall impedance
θ	angle of incidence (azimuth)
λ	wavelength, Courant number
ϵ	porosity
δ	end correction factor, scattering coefficient
T	reverberation time, time step
E	energy
a	specular absorption coefficient
d	diffusion coefficient
L	sound pressure level
X	internodal distance
f_s	sampling frequency
ϕ	angle of incidence (elevation)

Operators

Δ	Laplacian
∂	partial derivative

Abbreviations

ARD	Adaptive Rectangular Decomposition
ART	Acoustic Radiance Transfer
BEM	Boundary Element Method
DC	Direct Current
DCT	Discrete Cosine Transform
DWM	Digital Waveguide Mesh
FEM	Finite Element Method
FDTD	Finite-Difference Time-Domain
FFT	Fast Fourier Transform
GPU	Graphics Processing Unit
PML	Perfectly Matched Layer
SRL	Standard Rectilinear
TED	Temporal Envelope Distorting
TEP	Temporal Envelope Preserving

1   Introduction

The way sound waves react on contact with various materials, shapes and structures, is of fundamental interest in acoustics. It is of concern in architectural design, customization of auditorium and room acoustics, and in design of convincing auralizations of acoustical situations for virtual reality applications. The materials, shapes and structures determine the way sound energy is absorbed, reflected or transmitted, and the extent and quality of the spatial and temporal dispersion inherent in the reflections. These factors then contribute to a range of perceptually important acoustic properties such as the reverberation time of the space, the diffuseness of the sound field, and generally the way a sound source is translated through the acoustic space to a listener.

In most practical situations, the first reflections from surfaces arrive to the listener within a time and level that they are not perceived as separate sound events, or echoes, but rather the reflections fuse with the direct sound to form a single sound event. This perceptual phenomenon of integration is called the Haas effect [1] and it is an important area of study in psychoacoustics as it pertains to how e.g. music is experienced in concert halls. The relative levels of the direct and reflected sound and the delay between them, along with other factors such as the direction of arrival and the frequency-dependent and time-dispersive effects imposed by the reflective wall, determine the perceptual quality of the phenomenon. The nature of the early reflections inherent in an acoustic space is therefore an instrumental factor in determining the way sound is perceived.

Traditionally, the acoustic properties of enclosed spaces have been investigated using acoustic measurement methods, i.e. setting up one or more loudspeakers in an acoustic space to provide a sound source and recording the resultant sound with one or more microphones at selected locations. In this way, the transmission characteristics of the space are captured in the obtained impulse responses and further analysis can provide useful insights into its acoustics.

An important application is the prediction of acoustics of spaces prior to construction. Scale model techniques have been developed for this purpose and they involve construction of a scaled down model of the space (e.g. one-tenth of the original size) and executing the acoustic measurements in a proportionally higher frequency range. Selecting the materials for the scale model requires careful consideration in order that the right acoustic qualities be obtained for the higher frequencies. Similarly, the transmission medium must be chosen to approximate the absorption characteristics of air. Typically, either nitrogen or dried air is used as a substitute for regular air [2]. The drawback of the scale model technique is that the construction of models can be expensive and laborious.

Synthesizing the responses in a simulation environment has several benefits over doing measurements in a real acoustic space. Background noise, a nuisance in every conventional measurement, does not exist in simulations. It is also easy to replicate the measurement setting exactly and obtain the same results, unlike in a real situation where it is practically impossible to ensure that every detail is unchanged. Additional advantages are the lower material expenses and the ability to obtain re-

sults faster. The downside of simulations is that they are at best still only limited approximations of the physical reality and the computational and memory demands may get very high when a wide bandwidth and/or high modelling accuracy is needed.

Acoustic modelling methods can be divided into two main categories: geometric methods and wave-based methods. The geometric methods model the sound as sound rays that travel along straight paths and are specularly or diffusely reflected whenever a reflecting surface is met. The sound ray assumption is a sufficient approximation at high frequencies, for which the wavelengths are small compared to the obstacles typically found in an acoustic space. However, at low frequencies the assumption of straight paths is rendered invalid by the lack of modelling edge diffraction effects. Many geometric methods, e.g. ray tracing, are also based on calculation of energies rather than pressures, which results in neglect of interference effects. On the other hand, the wave-based methods are based on discretization of the wave equation and model the wave nature of sound directly, which inherently includes the diffraction effects as well as interference. The challenge of wave-based methods lies in the heavy computational and memory requirements that often restrict the bandwidth of practical simulations to well below the upper limit of human hearing.

1.1   The purpose of this thesis

The aim of this thesis is to provide qualitative insight into the ways in which layered wall structures affect incident sound. The effect of various structural features on the reflection characteristics are examined through the use of frequency- and time-domain analysis, visualizations and polar response measurements. The studied models are based partly on practical structures, e.g. structures found in concert halls, and partly on experimentation. The investigations were done by means of simulations using the standard rectilinear (SRL) finite-difference time-domain (FDTD) method for acoustics modelling in 2-D and 3-D. FDTD belongs to the category of time-domain wave-based methods and is capable of producing physically relevant results, with certain well-known limitations. The models for the simulations were designed with Google SketchUp [3] and a software developed for research purposes was used for the FDTD simulations.

1.2   Structure

The structure of the thesis is as follows. Section 2 presents the background for relevant phenomena in acoustics alongside measurement techniques and a brief introduction to various acoustic modelling methods. Section 3 introduces the 3-D version of the SRL FDTD method employed in this thesis and Section 4 presents introductory simulations and considerations concerning the simulation setup. Section 5 presents the simulations and results that form the main body of this work and Section 6 concludes the thesis.

2 Background

This section presents some of the relevant background in acoustics. Important concepts and phenomena pertaining to sound propagation in enclosed spaces are discussed and a few common measurement methods for acoustic coefficients for surface characterization are presented. The section concludes with a brief introduction of various acoustic modelling methods.

2.1 Sound in enclosed spaces

This section discusses the propagation of sound in enclosed spaces. The two elementary wave types of special importance, plane waves and spherical waves, are discussed. The theory behind sound interaction with surfaces is introduced in the form of a plane wave incident on a flat surface extending to infinity. The phenomena of surface scattering, diffraction and resonance are also briefly discussed. The sections concerning the elementary wave types and reflection from a flat surface follow closely the discussions given in [1].

2.1.1 Plane waves

Sound wave propagation in a lossless fluid is governed by the wave equation

$$c^2 \Delta p = \frac{\partial^2 p}{\partial t^2} \; , \tag{2.1}$$

where Δ is the Laplacian, c is the speed of sound, p is the sound pressure and t is the time. For a plane wave, the sound pressure is a function of time and one spatial variable (the direction normal to the plane wave) and every planar front whose normal is parallel to the direction of travel has constant pressure and is therefore called a *wavefront*. To produce such a wave, a source of infinite dimensions is needed. Thus, in reality only waves that are approximately planar exist. For a plane wave propagating in the direction parallel to the x-axis, equation (2.1) can be written as

$$c^2 \frac{\partial^2 p}{\partial x^2} = \frac{\partial^2 p}{\partial t^2} \; . \tag{2.2}$$

A general solution to this differential equation is

$$p(x,t) = F(ct - x) + G(ct + x) \; , \tag{2.3}$$

where F and G are arbitrary functions with existing second order derivatives. F represents a wave travelling to the positive x-direction and G represents a wave travelling to the negative x-direction. The particle velocity has only one component, parallel to the direction of travel, and it is expressed as

$$v(x,t) = \frac{1}{\rho_0 c}[F(ct - x) - G(ct + x)] \; , \tag{2.4}$$

where ρ_0 is the density of the surrounding fluid. From equations (2.3) and (2.4) it can be seen that for a plane wave travelling in the positive direction (G = 0) the ratio of sound pressure and particle velocity is independent of frequency:

$$\frac{p}{v} = \rho_0 c \; . \tag{2.5}$$

This ratio is the *characteristic impedance* of the medium. Setting $G = 0$ in equation (2.3), adding a harmonic time and space dependency (cosine function) and using complex notation leads to

$$p(x,t) = \hat{p} e^{i(\omega t - kx)} \; , \tag{2.6}$$

where $\hat{p}$ is the amplitude (peak value) of the pressure, $\omega = 2\pi f$ is the angular frequency and $k = 2\pi f/c$ is the wavenumber.

2.1.2 Spherical waves

For a spherical wave, the pressure is uniformly distributed over a sphere. Instead of the cartesian coordinate system, a more natural domain to consider spherical waves is within the spherical coordinate system. The sound pressure for a wave of this type depends on time and the distance from the source point, and equation (2.1) can thus be written as

$$\frac{\partial^2 p}{\partial r^2} + \frac{2}{r}\frac{\partial p}{\partial r} = \frac{1}{c^2}\frac{\partial^2 p}{\partial t^2} \; , \tag{2.7}$$

where r denotes the distance from the source. A spherical wave is produced by a source that is small compared to the wavelength, i.e. a point source, that introduces or withdraws fluid with volume velocity Q. A solution to equation (2.7) is

$$p(r,t) = \frac{\rho_0}{4\pi r}\dot{Q}\left(t - \frac{r}{c}\right) \; , \tag{2.8}$$

where $\dot{Q}$ is the partial derivative of the volume velocity with respect to time. The only component of the particle velocity is radial and it reads as

$$v_r = \frac{1}{4\pi r^2}\left[Q\left(t - \frac{r}{c}\right) + \frac{r}{c}\dot{Q}\left(t - \frac{r}{c}\right)\right] \; . \tag{2.9}$$

Adding a harmonic time variation to the volume velocity Q in equation (2.8), i.e. $Q(t) = \hat{Q}e^{i\omega t}$, gives

$$p(r,t) = \frac{i\omega\rho_0}{4\pi r}\hat{Q}e^{i(\omega t - kr)} \; . \tag{2.10}$$

The particle velocity is now

$$v_r = \frac{p}{\rho_0 c}\left(1 + \frac{1}{ikr}\right) \; . \tag{2.11}$$

Solving for p/v_r gives

$$\frac{p}{v_r} = \frac{\rho_0 c}{1 + 1/ikr} \; . \tag{2.12}$$

In contrast to the case with the plane wave (see equation (2.5)), it is evident from equation (2.12) that for a spherical wave the ratio of sound pressure and particle velocity is complex (i.e. there is a phase difference) and that it depends on the distance as well as the frequency. This observation leads to a distinction between the *near field* and the *far field* [4]. For distances that are large compared to the wavelength ($kr \gg 1$), the value of equation (2.12) tends towards the characteristic impedance of the medium $\rho_0 c$. At such distances, a small region of a spherical wave can be considered a good approximation of a plane wave and the region is considered to be in the *far field* for that wavelength. On the other hand, at distances that are small compared to the wavelength ($kr \ll 1$), there is a large particle velocity component out of phase with the pressure. It is a source of additional reactive energy that stays close to the source and does not radiate outward [4]. The region in which this holds is considered the *near field*.

Figure 2.1 shows the absolute value of the ratio of p/v_r at various $frequency \times distance$ values and how it approaches the characteristic impedance of the medium. For instance, at a frequency of 200 Hz a spherical wave may be considered an adequate approximation of a plane wave for path distances over 2 m ($f \cdot r = 400$) from the source point.
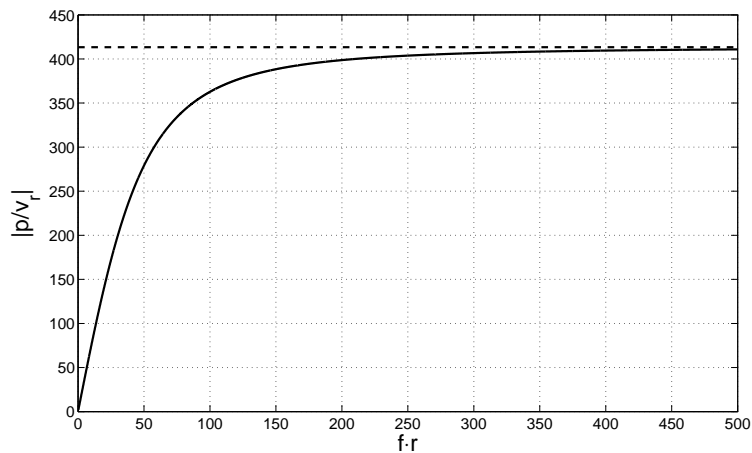
Figure 2.1: The absolute value of the p/v_r ratio (solid line) for various values of $f \cdot r$; $c = 343.26$ m/s and $\rho_0 = 1.2041$ kg/m^3 (air at a temperature of 20°C); the corresponding characteristic impedance (dashed line) is shown for reference.

2.1.3 Reflection at a boundary

In this section, a plane wave is assumed although in reality all sound waves are more or less spherical in nature due to the sources being finite. An infinite wall geometry is also assumed to discount any edge diffraction effects. A plane wave incident upon a uniform wall may be partly reflected and partly absorbed. The reflection properties of the wall are characterized by the complex reflection coefficient

$$R = |R|e^{i\varphi} \ , \tag{2.13}$$

where $|R|$ specifies the amplitude change and φ the phase change that occurs in the reflection. Both depend on the angle of incidence as well as the frequency. The fraction of energy lost during the reflection is expressed by the absorption coefficient

$$\alpha = 1 - |R^2| \; . \tag{2.14}$$

A given sound pressure at the surface of a wall generates a particle velocity normal to the surface. The ratio of the sound pressure to the generated normal particle velocity is called the wall impedance:

$$Z_w = \frac{p}{v_n} \; . \tag{2.15}$$

The impedance is generally complex valued and a function of the angle of incidence. The specific wall impedance is defined as

$$\xi_w = \frac{Z_w}{\rho_0 c} \; , \tag{2.16}$$

where $\rho_0 c$ is the characteristic impedance of the surrounding medium. Assuming a plane wave travelling along the x-axis normal to a uniform wall surface ($x = 0$ at wall boundary), the sound pressure of the incident wave coming towards the wall is governed by

$$p_{inc}(x,t) = \hat{p}_0 e^{i(\omega t - kx)} \; , \tag{2.17}$$

where $\hat{p}$ is the amplitude of the wave, $\omega = 2\pi f$ is the angular frequency and $k = 2\pi f/c$ is the wavenumber. Making use of the fact that for a plane wave $p/v = \rho_0 c$, the corresponding particle velocity is

$$v_{inc}(x,t) = \frac{\hat{p}_0}{\rho_0 c} e^{i(\omega t - kx)} \; . \tag{2.18}$$

Similarly, the sound pressure and the particle velocity for the reflected wave are

$$p_{ref}(x,t) = R\hat{p}_0 e^{i(\omega t + kx)} \tag{2.19}$$

and

$$v_{ref}(x,t) = -R\frac{\hat{p}_0}{\rho_0 c} e^{i(\omega t + kx)} \; , \tag{2.20}$$

respectively. At the wall boundary ($x = 0$), the sound pressure and particle velocity are superpositions of the incident and reflected waves:

$$p(0,t) = (1 + R)\hat{p}_0 e^{i\omega t} \tag{2.21}$$

$$v(0,t) = (1 - R)\frac{\hat{p}_0}{\rho_0 c} e^{i\omega t} \; . \tag{2.22}$$

Dividing equation (2.21) by (2.22) gives the wall impedance

$$Z_w = \rho_0 c\frac{1 + R}{1 - R} \; . \tag{2.23}$$

Applying this result to equation (2.16) gives the specific wall impedance

$$\xi_w = \frac{1+R}{1-R} \; .$$

(2.24)

Solving for the reflection coefficient R gives

$$R = \frac{\xi_w - 1}{\xi_w + 1} \; .$$

(2.25)

The plane wave reflection coefficient for oblique incidence can be obtained following a similar procedure (which is given in detail in [1] but left out here for brevity) and leads to

$$R(\theta) = \frac{\xi_w \cos\theta - 1}{\xi_w \cos\theta + 1} \; ,$$

(2.26)

where θ is the angle of incidence, signifying deviation from the normal of the surface.

2.1.4 Scattering

In practice, surfaces are never completely flat and exhibit irregularities. These surface features have an effect on the reflection of the incident wave depending on the relation of the feature dimensions to the wavelength. Figure 2.2 shows the three principal cases. In case (a), the wavelength of the incident wave is much larger than the surface irregularities, and the surface reflects the wave in the same manner as a flat surface. In case (c), the wavelength is much smaller than the surface features, which can then be considered as series of oriented flat surfaces that reflect the wave specularly. In case (b), the wavelength and the dimensions of the surface irregularities are of comparable magnitude. In this case the incident wave is scattered to various directions, depending on the surface geometry, and the exact behaviour of the reflections is harder to predict.
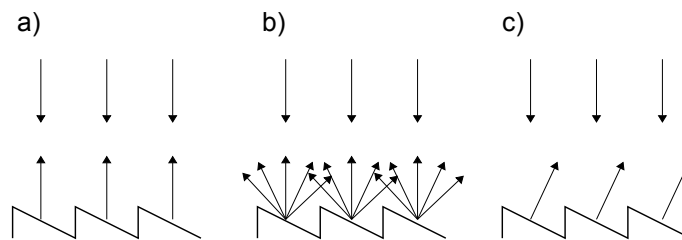
Figure 2.2: Reflection by a rough surface: a) $d \ll \lambda$ b) $d \approx \lambda$ c) $d \gg \lambda$.

It is evident that the reflection and absorption coefficients – as defined in the previous section – are inadequate at describing the complexity of the acoustic behaviour of scattering surfaces. For this reason two coefficients, the *scattering coefficient* and the *diffusion coefficient*, have been developed [5]. Both of them aim at characterizing the scattering properties of surfaces but have different physical meaning and purpose.

The *scattering coefficient* is motivated by the need to quantify the portion of non-specularly reflected sound energy for geometric modelling methods. The inclusion of scattering effects has been found to be instrumental in improving the predictive quality of these methods [6]. In particular, room acoustics simulation using geometric methods that neglect scattering effects tend to overestimate the reverberation time of spaces. This is especially true when absorption is unevenly distributed among surfaces. The scattering coefficient is the ratio of the scattered sound to the total reflected sound and it is used to decide whether a reflection is specular or diffuse. The exact direction of scattering for a reflection is determined by a spatial distribution such as Lambert's cosine law [1]. The scattering coefficient is angle- and frequency-dependent and is uniquely specified for 1/3 octave or octave frequency bands. A random-incidence scattering coefficient can be obtained by averaging the scattering coefficients over different angles of incidence. Section 2.2.3 describes methods for obtaining scattering coefficients.

The *diffusion coefficient* quantifies the degree of uniformity of the polar response of a surface. It has been developed primarily to serve as a quality measure of diffusers, i.e. surfaces designed to diffuse sound energy within a specific bandwidth, but it can also be used to characterize diffusing properties of other surfaces. Diffusers are used e.g. on back walls in large auditoria for preventing disturbing echoes and for reducing coloration due to standing waves in small sound reproduction rooms. A variety of different design principles exist, but generally all of them aim at fulfilling the same criterion: an ideal diffuser produces within its operational bandwidth a polar response that is invariant to the angle of incidence, angle of observation and frequency [7]. A diffusion coefficient value of one means that the surface scatters sound energy uniformly in all directions, whereas a coefficient value near zero means that all the energy goes to one direction. The diffusion coefficient is angle- and frequency-dependent and uniquely specified for each 1/3 octave band. A method for obtaining diffusion coefficients is presented in section 2.2.4.

The common deficiency of both the diffusion coefficient and the scattering coefficient is that they do not convey any information about the temporal spreading effects of surfaces on sound. For example, in concert halls temporal envelope preserving (TEP) lateral reflections have been found to be an important factor in creating a sense of envelopment in the music listening experience [8]. In contrast, the temporal envelope distorting (TED) reflections partially break the precedence effect, which is a crucial part of forming the perceived sound image within the human auditory system. A complete assessment criteria for scattering surfaces must therefore include a way to also characterize their effects on the temporal envelope of the reflected sound.

2.1.5 Diffraction

Diffraction is the phenomenon of waves bending around obstacles. The effect is most pronounced for wavelengths for which the object dimensions are of a similar order of magnitude. The laws of physics require that the pressure field is continuous at all points and diffraction is the phenomenon that ensures this continuity when
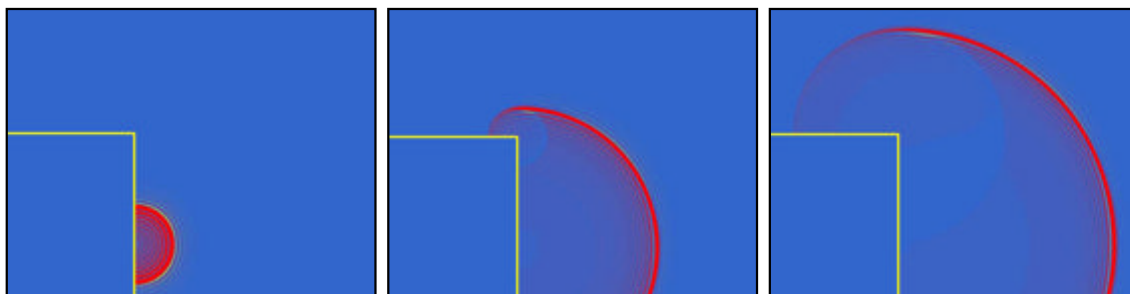
Figure 2.3: A 2-D FDTD simulation showing the diffraction effect around a corner.

the wavefront is chopped by various obstacles. Figure 2.3 depicts the diffraction effect with snapshots of a 2-D FDTD simulation. The source is positioned at the boundary. As the wave propagates past the edge of the wall, the diffraction effect is seen to compensate for the cutting effect of the corner. Thus, the wavefront is fully continuous even in the shadow region where there is no direct path to the source. In practice this means that in many real situations, sound can be heard even if no direct or specular reflection paths can be found. Modeling diffraction is therefore crucial for realistic auralization, especially in cases where the direct path to the sound source is occluded and there are no reflection paths that reach the receiver. A situation like this can occur for instance in simulations of outdoor situations. Then the diffraction around edges is the only phenomenon that can provide the receiver with auditory information about the source.

2.1.6 Resonance

This section discusses acoustic resonance. Resonances give to acoustic sources their signature timbral characteristics. However, in acoustic spaces where accurate and pleasant sound transmission is the primary objective, structural resonances can be problematic. Such resonances may introduce coloration that is manifested as notches or peaks within the sound spectrum. In the following, a few common mechanisms for acoustic resonances are discussed.

Resonances in tubes

In a tube (or pipe or duct), sound propagates as a plane wave if the dimensions of the tube are small compared to the wavelength. When the propagating wave is incident on an impedance boundary, it is more or less reflected. The proportion of sound that is reflected is dependent on the relation of the impedances of the two domains. A large impedance difference leads to a large proportion of the sound being reflected and vice versa. The boundary condition for a hard boundary requires that the change in pressure with distance is zero at the boundary. A pressure release boundary condition, on the other hand, requires that the pressure goes to zero at the boundary. Successive reflections between two ends of a tube gives rise to resonances for frequencies at which the reflected waves interfere in phase. At these frequencies, standing waves are formed within the tube. The other frequencies tend to cancel

each other and average out to zero amplitude. For a closed-closed or an open-open tube, the resonant frequencies are given by [9]

$$f_n = \frac{nc}{2l} \ , \tag{2.27}$$

where $n = 1, 2, 3, \ldots$ and l is the length of the tube. The difference between these two cases is that in the open ended tube, the pressure maximum in the fundamental frequency is at the middle of the tube rather than at the ends. This is because the ends are of the pressure release type. In practice, however, the open ends have finite impedances and thus the pressure is not exactly zero. In order to accommodate for this, end corrections are required for the open-open tube that give the acoustical length of the tube, which is longer than the actual physical length. Finally, for a tube with one closed and one open end, the resonant frequencies are given by [9]

$$f_n = \frac{(2n-1)c}{4l} \ , \tag{2.28}$$

where $n = 1, 2, 3, \ldots$ and l is the length of the tube.

Helmholtz resonator

Many mechanical systems exhibit forces that restore the system to equilibrium after initial displacement. A plucked string and a simple spring-mass system are examples of this behaviour. When the spring-mass system is released from the state of initial displacement, it oscillates between two extremes at regular intervals until the restoring force of the spring is extinguished and the system is back at equilibrium. The frequency corresponding to the regular interval of the motion is the resonance frequency of the system and it is dependent both on the mass and the stiffness of the spring.

An enclosed volume of air can also act as the spring of a spring-mass system. The air in the opening(s) to such volume then acts as the mass of the system. Therefore structures with cavities exhibit acoustical resonances. Understanding the acoustic resonance phenomena is thus instrumental to understanding the acoustical properties of wall structures with cavities. An important concept in acoustics is the Helmholtz resonator, shown in Figure 2.4, in which an enclosed air-spring is compressed by a piston of air in a neck opening acting as the mass. The stiffness of the air spring is determined by the total volume while the shape of the volume is arbitrary. The resonance frequency of the system is [9]

$$f = \frac{c}{2\pi} \sqrt{\frac{S}{Vl}} \ , \tag{2.29}$$

where V is the volume of the enclosed air, S is the area of the neck and l its length. Helmholtz resonators are used for instance in bass-reflex loudspeakers and as bass traps. Forming a Helmholtz resonator out of a loudspeaker cabinet extends the low frequency range of the loudspeaker by tuning the enclosure in such a way as to facilitate low frequency emission near the resonance frequency. In contrast, a bass

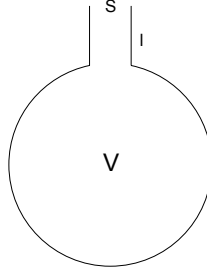trap is tuned to absorb selected frequencies and typically used to alleviate unwanted room resonances.

Figure 2.4: A Helmholtz resonator.

Distributed Helmholtz resonators

A structure with an air volume with openings in the form of multiple holes or slats is called a *distributed Helmholtz resonator* [10]. These structures are typically used to form tuned resonant absorbers by applying a layer of porous material in the cavity, e.g. right behind the panel, to provide a loss mechanism that converts sound energy into heat. Figure 2.5 shows cross-sections of two types of such structures. For both structures, the resonant frequency can be calculated with

$$ f = \frac{c}{2\pi} \sqrt{\frac{\epsilon}{l(d + \Delta d)}} \ , \tag{2.30} $$

where l is the cavity depth, d is the panel thickness and $\epsilon = S/S_0$ is the 'porosity', i.e. fraction of open area, in the panel. S and S_0 are the total sum of open area in the panel and the full area of the panel, respectively. $\Delta d = 2a\delta = b\delta$ is the end correction for the length of the 'air plugs' and it depends on the geometry of the openings. Here a denotes the radius of a circular opening and b the width of a square hole/slat opening. There is some ambiguity in the literature in regard to the appropriate end corrections for various openings and generally a single definitive answer can not be found. For holes, one end correction factor is given in [7] as

$$ \delta = 0.8(1 - 1.47\epsilon^{1/2} + 0.47\epsilon^{3/2}) \ . \tag{2.31} $$

It is assumed here that equation (2.31) is an end correction factor for *circular* holes, although it is not explicitly mentioned in the reference. For *square* holes, using an effective diameter of $1.13b$ is recommended in [11]. For slat openings the end correction is given in [10] as

$$ \Delta d = -\frac{2b}{\pi} \ln \left[\sin \left(\frac{\pi\epsilon}{2} \right) \right] \ . \tag{2.32} $$

The resonance frequency of the structure can be tuned to a desired frequency by varying the design parameters.
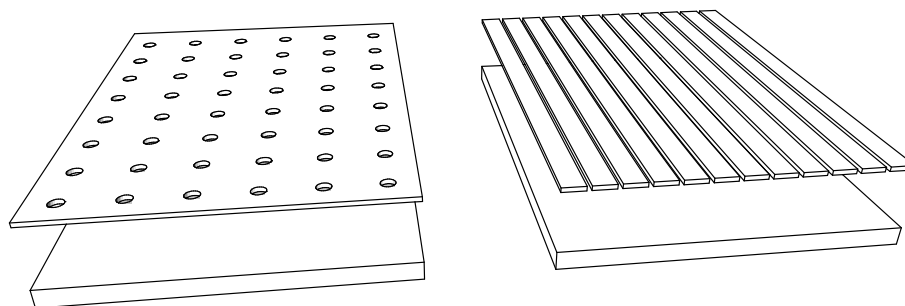
Figure 2.5: Distributed Helmholtz resonators (cross-section). Left: a panel with holes backed by a cavity; right: a panel with slats backed by a cavity.

2.2 Measurement methods for room acoustic coefficients

This section presents acoustical measurement methods for obtaining the absorption, scattering and diffusion coefficients for a variety of materials and surfaces.

2.2.1 The impedance tube method

In the impedance tube method, a tube with a rectangular or circular cross-section is used to carry out measurements that yield the normal-incidence absorption coefficient for a small sample of absorptive material. The surface of the material should be approximately flat and the material is assumed to be locally reacting, i.e. the normal component of the particle velocity at an element of the surface is only dependent on the pressure at that element and not on the pressure at neighbouring elements [1].

At one extreme of the tube, a loudspeaker provides the sinusoidal source signal for the measurement. Absorbing termination may be added to the front of the loudspeaker to alleviate unwanted tube resonances. At the other extreme, the tube is rigidly terminated and the test sample is situated near the end, albeit slightly removed from the rigid termination in order to resemble practical applications of the material. Practical applications here refer to the fact that ideally, wall mounted absorber panels should be installed in a way that leaves a gap between the panel and the hard surface. This is because a sufficient particle velocity is a prerequisite for efficient absorption and the particle velocity at the surface of a hard wall is zero. Figure 2.6 shows a schematic of an impedance tube.

The principle of the method is that when the source signal and the reflected sound interfere in the tube, a standing wave is formed. A movable probe microphone, small enough to be acoustically transparent in the measurement context, is used to search for the pressure maxima and minima of the standing wave. The normal incidence reflection coefficient can then be determined from the values and locations of the pressure minima and maxima. The tube should be long enough to accommodate at least one pressure minimum and maximum at the lowest frequency of interest. The lateral diameter of the tube should satisfy
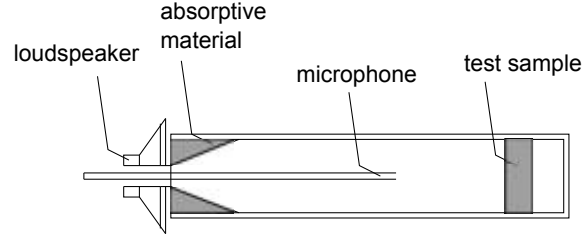
Figure 2.6: A schematic diagram showing the principal structure of the impedance tube.

- $d_{longest} < 0.5\lambda_{min}$ (for rectangular cross-section)

- $d < 0.586\lambda_{min}$ (for circular cross-section)

to avoid any lateral propagation of waves in the tube. On the other hand, the lateral dimensions should not be too small as the attenuation due to losses at walls may become prohibitively high. In practice, at least two tubes with different dimensions are needed to cover a range from about 100 Hz to 5 kHz.

By measuring the maximum and minimum values of the sound pressure in the tube, the absolute value of the normal incidence reflection coefficient, and the normal incidence absorption coefficient can be obtained from

$$|R_n| = \frac{\hat{p}_{max} - \hat{p}_{min}}{\hat{p}_{max} + \hat{p}_{min}} \tag{2.33}$$

and

$$\alpha_n = \frac{4\hat{p}_{max} \cdot \hat{p}_{min}}{(\hat{p}_{max} + \hat{p}_{min})^2} \ , \tag{2.34}$$

respectively. From the location of the first pressure maximum near the test sample, the phase change φ of the reflection can be calculated using

$$\varphi = \pi\left(1 - \frac{4x_{min}}{\lambda}\right) \ , \tag{2.35}$$

where x_{min} is the distance from the sample to the nearest pressure maximum and λ is the related wavelength. The complex reflection coefficient can be reconstructed from equations (2.33) and (2.35) and can then be used to obtain the impedance or specific impedance for the test sample using equation (2.23) or (2.24), respectively. [1]

2.2.2 The reverberation chamber method

The reverberation chamber method is used for measuring the absorption by materials and objects in a diffuse field, i.e. where the sound pressure variance is (near) zero and energy density is (nearly) the same for all positions. For the method, a room of at least 100 m^3 volume is needed. The walls of the chamber should be as uniform,

rigid and smooth as possible. The absorption coefficient α_0 for the chamber walls can be obtained from the reverberation time of the chamber [1]

$$T_0 = 0.161 \frac{V}{S\alpha_0} \; , \tag{2.36}$$

where V is the volume of the chamber and S the wall area. Introducing a test sample to the chamber reduces the reverberation time to

$$T = 0.161 \frac{V}{S_s\alpha_s + (S - S_s)\alpha_0} \; , \tag{2.37}$$

where S_s and α_s are the surface area and random-incidence absorption coefficient of the test sample. The absorption coefficient for the test material can be found from this result. The effect of air absorption can be neglected as it will be nearly equal in the measurements done in the empty chamber and with the test sample intact.

In a completely diffuse field, the reverberation time measurements would provide the exact same results for different microphone positions in the room. In practice, the sound field is only relatively diffuse and the measured reverberation time changes depending on the position. Therefore, the measurements should be carried out in various positions and the results averaged to ensure more accurate results. The advantage of the reverberation chamber method is that the test samples can easily be mounted in their application specific way. Also, the total absorption by discrete objects that cannot be characterized by an absorption coefficient, i.e. chairs, can be measured. In that case, $S_s\alpha$ in equation (2.37) is replaced by the total absorption of the object(s). [1]

2.2.3 Methods for obtaining scattering coefficients

The two methods presented here are derived from [12]. For a single reflection from a scattering surface, the specularly reflected energy can be expressed as

$$E_{spec} = (1 - \alpha)(1 - \delta) = 1 - a \; , \tag{2.38}$$

where α is the absorption coefficient, δ is the scattering coefficient and a is the 'specular absorption coefficient', i.e. the portion of energy lost from the specular reflection direction due to both scattering and absorption. The total reflected energy from the surface is

$$E_{total} = 1 - \alpha \; . \tag{2.39}$$

Using (2.38) and (2.39), the scattering coefficient can be obtained with

$$\delta = \frac{a - \alpha}{1 - \alpha} = 1 - \frac{E_{spec}}{E_{total}} \; . \tag{2.40}$$

The principle is to obtain the specular component E_{spec} by phase-locked averaging of results obtained for various sample orientations. It is based on the observation that for a circular sample of rough surface, with varying orientation (rotation along the axis that goes through the center of the sample), the reflected sound will be

highly correlated for the early (specular) part. The later (scattered) part of the reflection varies significantly for different sample orientations. When a sufficiently large amount of results for different sample orientations are summed and averaged, the specular parts add up constructively and the scattered parts tend to average to zero.

In the *free-field method*, the first step in obtaining an angle-dependent scattering coefficient is to determine the complex reflection factors for different sample orientations. The reflection factor can be expressed as a sum of the specular and diffuse components with

$$R_i(f) = R_{spec}(f) + S_i(f) \ , \tag{2.41}$$

where R_{spec} is the specular component of the reflection, which stays approximately same for all sample orientations, and S_i is the diffuse component. The subscript i numbers the different sample orientations and f denotes the frequency. By averaging a sufficiently large amount of responses, the specular component can be obtained with

$$R_{spec}(f) \cong \frac{1}{n} \sum_{i=1}^{n} R_i(f) \ . \tag{2.42}$$

The specular absorption coefficient is then calculated with

$$a(f) = 1 - |R_{spec}(f)|^2 \ , \tag{2.43}$$

which is equal to the scattering coefficient δ under the condition that the energy losses are small enough to be neglected. If this condition is not fulfilled, the absorption coefficient must be determined separately. A random-incidence scattering coefficient can be calculated by taking the specular absorption coefficients obtained for different angles of incidence and applying them to Paris' formula [1]:

$$\alpha_r = \int_0^{\pi/2} \alpha(\theta) \sin(2\theta) d\theta \ , \tag{2.44}$$

where θ is the angle of incidence.

The *reverberation chamber method* of obtaining the scattering coefficient is based on the same principle of phase-locked averaging of results for different sample orientations. However, instead of an angle-dependent scattering coefficient it yields the random-incidence scattering coefficient directly, with considerably less laborious measurements. It is enough to obtain a result for only one reflection angle θ for each sample orientation. The principle is that if the sample introduces scattering, the room impulse responses will have slightly different fine structures for various orientations of the sample. However, the average energy decay is the same for all orientations. By averaging over a sufficient amount of measurements, the differences (due to scattering) tend to average to zero and the average energy decay can be obtained. This entails the assumption that the specular and scattered components are statistically independent. Addition of n room impulse responses allows approximation of the energy decay $E(t)$ as

$$E(t) = (n-1)e^{(cS/4V)ln(1-\bar{a})t} + e^{(cS/4V)ln(1-\bar{\alpha})t} \ , \tag{2.45}$$

where $\bar{a}$ is

$$\bar{a} = \frac{1}{S}[(S - S_s)]\alpha_0 + S_s a_s] \; , \tag{2.46}$$

with S_s being the surface area of the sample, a_s the specular absorption coefficient for the sample and α_0 the mean absorption coefficient for the empty chamber. For sufficiently large n the latter exponential function in equation (2.45) can be neglected. A reduced reverberation time (see (2.37)) can be obtained through evaluation of the early part of $E(t)$. The absorption coefficients α_s and a_s can then be determined with equations (2.37) and (2.45), respectively, and the random incidence scattering coefficient δ_s is finally obtained through equation (2.40).

2.2.4 A method for obtaining the diffusion coefficient

The method presented here is discussed in [7] and thoroughly instructed in the AES-4id-2001 standard document [13]. The process of obtaining a diffusion coefficient for a surface starts by investigating the spatial distribution of scattered energy for various angles of incidence. This is achieved through radiating a source signal to the test sample and recording the responses at various angles, i.e. $-90°$ to $90°$ in $5°$ increments (37 receiver positions/semicircle) for azimuth/elevation angles, depending on whether the measurements are done over a semicircle or a hemisphere. The measurements are then repeated for various source positions, likewise mapping out a semicircle or a hemisphere, at a maximum of $10°$ separation. Figure 2.7 shows a schematic drawing of the measurement setup for measuring the polar response over a semicircle with $5°$ separation used between adjacent source and receiver positions.

The measurements need to be conducted in the far field so that the majority of receivers are outside the specular reflection zone, i.e. the portion of the receiver arc or hemispherical surface that is between the furthest specular reflection paths from the sample (see Figure 2.7). This is because the object of the measurements is to quantify the extent to which a surface directs the sound energy away from specular directions. If the receivers are too close to the sample surface, even the responses from a flat panel will give high diffusion coefficient values. The recommendation is that for a full scale measurement geometry, the source should be situated 10 meters and the receiver arc 5 meters from the sample, and at least 80% of the receivers should be situated outside the specular zone [13].

For surfaces that scatter in a single plane, measuring the polar response over a semicircle is adequate. For surfaces that scatter in multiple planes, the measurements should ideally be taken over a hemisphere. As hemispherical measurements can be difficult and time-consuming to carry out, a couple of single plane measurements made in orthogonal directions may suffice. Possible symmetry in the sample can also be exploited to reduce the number of measurements needed for the hemispherical measurements. Due to the complexities involved in performing a full-scale hemispherical measurement, use of prediction tools such as the boundary element method (BEM) is an attractive alternative to physical measurements.

The polar response measurements are generally carried out in an anechoic chamber. For single plane measurements, the boundary plane measurement technique
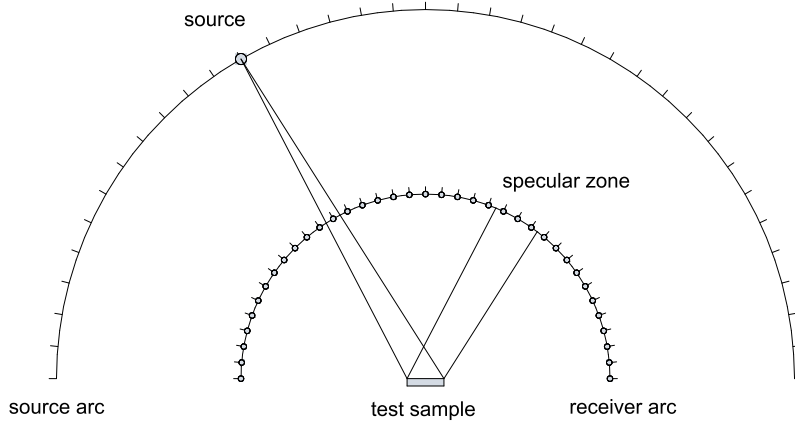
Figure 2.7: Measurement of the polar response of a surface over a semicircle.

– where the source, receivers and test sample are situated on a hard and smooth boundary plane – is a viable alternative. The precondition is that the ceiling and walls should be far enough removed from the test setup to enable proper isolation of the target reflections in the time domain. In practice, whether the measurements are taken in an anechoic chamber or using the boundary plane technique, scale models (e.g. 1:5) have to be used since otherwise the required measurement setup geometry becomes prohibitively large.

In addition to the actual test sample responses, the process involves measuring the background response (without the test sample) for all the source/receiver combinations. The reflection response is then obtained in isolation through subtraction of the background response from the test response and applying appropriate windowing. The individual receiver response energies are obtained for each 1/3 octave band and combined to form the 1/3 octave band polar responses for a particular angle of incidence. An autocorrelation diffusion coefficient is then calculated with

$$d_\theta = \frac{(\sum_{i=1}^{n})10^{L_i/10})^2 - \sum_{i=1}^{n}(10^{L_i/10})^2}{(n-1)\sum_{i=1}^{n}(10^{L_i/10})^2} \; , \tag{2.47}$$

where L_i are sound pressure levels (in dB), n is the number of receivers and θ is the angle of incidence.

The final diffusion coefficient value is obtained by averaging the diffusion coefficient values over all angles of incidence. At this point, however, the diffusion at low frequencies is over-estimated because edge diffraction effects dominate due to the finite size of the sample. For this reason, the measurements are also carried out with a reference flat panel of equal dimensions. The normalized diffusion coefficient is then calculated by subtracting the values obtained for the flat panel from the diffusion coefficient:

$$d_{\theta,n} = \frac{d_\theta - d_{\theta,r}}{1 - d_{\theta,r}} \; . \tag{2.48}$$

Here $d_{\theta,r}$ is the diffusion coefficient value for the reference flat panel. The normalization procedure neutralizes the effect of edge diffraction on the diffusion coefficient. In case the normalization results in negative diffusion coefficient values for some
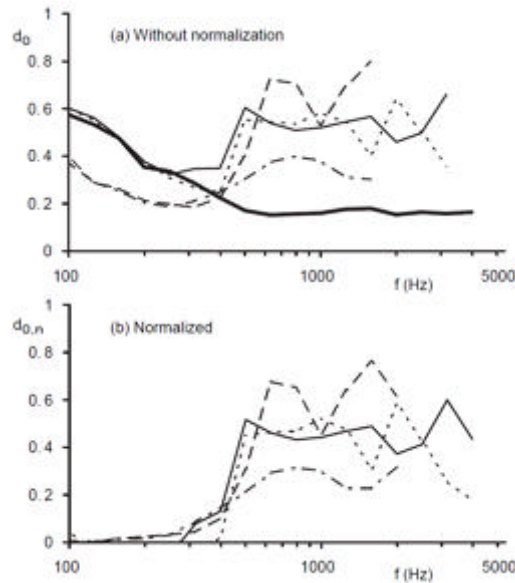
Figure 2.8: The effect of normalization on the diffusion coefficients for four commercial diffusers. The thick line in the top plot is the reference flat surface used for normalization. The figure is adopted from [7].

1/3 octave bands, these values should be manually rectified to 0. Figure 2.8 shows the effect of normalization on the diffusion coefficient values for four commercial diffusers.

2.3 Modelling of acoustic spaces

The field of research that concerns the modelling of acoustic spaces as well as the sources and receivers in them is often termed *virtual acoustics*. A branch of this field, *auralization*, aims at modelling the binaural listening experience at a given position in the modeled space [14]. For the purposes of this thesis, only the modelling of the medium and the structures within it is of interest. Consequently, issues related to the specifics of source and receiver characteristics, e.g. directivity, are left out of the discussion. Throughout the simulations in this thesis, the sources are invariably omnidirectional point sources and the receivers are merely acoustically transparent points where pressure fluctuations are recorded.

Acoustic modelling methods can be divided into two main categories: geometric methods and wave-based methods. The geometric methods decompose the sound field to elementary wave components and treat them as sound rays that travel along straight paths. In contrast, the wave-based methods aim to solve the total sound field by discretizing a suitable form of the wave equation. In principle, the wave-based methods model the sound field more accurately, but in practice the high computational demands severely limit the usable accuracy range of the methods. The geometric methods are generally less computationally demanding, and also more flexible in terms of customization of distribution of resources. From the point of

view of acoustic modelling, the choice of methods depends on the demands set by the target application, the available resources and the corresponding trade-off between accuracy and interactivity. For example, games and multimedia applications call for real-time simulation and plausible rather than accurate quality. In contrast, the prediction of acoustics in rooms can usually be computed offline but require high accuracy in order to produce physically relevant results.

The aim of acoustical simulations is to obtain the impulse response, or transfer function, that characterizes the sound transmission between a source and a receiver point in the space. For the wave-based methods, the computational complexity is the same throughout the calculation of the impulse response. For the geometric methods, the computational complexity generally becomes greater with increasing time as the number of distinct reflections in an enclosed space is roughly proportional to time squared [15]. An important point is that the early part of the impulse response is perceptually the most important due to the sparseness of early reflections and their importance in providing spatial cues for the human hearing system. The late part, on the other hand, is usually largely diffuse and so complex as to be perceptually indistinguishable from a statistical method of late reverberation.

A main challenge in acoustics modelling is that it is difficult to acquire high accuracy results by employing a single method for all purposes. For this reason, hybrid methods that use various methods for calculating different parts (time/frequency) of the impulse response have been studied. For example, a hybrid method that employs a 3-D digital waveguide mesh (DWM) for the early part of the low frequency impulse response calculation and a 2-D DWM for the late part, and ray-tracing for the high frequencies, has been studied in [16]. Furthermore, it has been proposed that a threefold method could combine the best of different methods: a wave-based method for low frequencies, an image source method for the early part, and an energy transfer/radiosity method for the late part of the response for mid and high frequencies. This approach would be beneficial in optimizing efficiency and accuracy [17]. One such method uses beam tracing for the early part, and acoustic radiance transfer (ART) for the late (diffuse) part for mid and high frequencies, and FDTD for low frequencies [18]. An overview of various simulation methods for calculation of the impulse response, as well as auralization, is given in [15].

2.3.1 Geometric methods

In geometric acoustics, sound is represented by sound rays that are assumed to travel along straight paths. The assumption can be considered valid in the high frequency range where the object dimensions in the space are generally much larger than the wavelengths. For longer wavelengths, however, it is invalid because the assumption of straight paths neglects all edge diffraction effects. The modelling of edge diffraction in geometrical acoustics requires the inclusion of special edge sources. In the following, common geometric modelling methods are briefly discussed. A unifying framework for the various geometric methods is given by the room acoustic rendering equation [19].

Image source method

The image source method [20] [21] finds the explicit paths for specular reflections in an enclosure. The principle is that a source near boundaries can be represented by the source and its virtual counterparts that are found by mirroring the source with respect to the boundaries. For obtaining secondary reflections, the first order image sources are mirrored again. The mirroring process is continued until the desired order of reflections is reached. Each image source must also be checked for validity and visibility. The image source is visible when the line of propagation from the image source to the receiver point intersects the boundary of reflection. Also, it must be checked that the path from the image source to the receiver is not occluded. The path lengths are used for appropriate scaling and delaying of the source signals at the receiver. Multiplying the source signals by the reflection coefficients of the walls enables a range of boundary conditions to be implemented. The boundary conditions of the space are thus fulfilled by the image sources and the actual boundaries can be neglected.

The number of possible image sources grows exponentially with the reflection order and the method is therefore practical only for modelling the early part of the impulse response. The validity and visibility checks can also get computationally heavy. A more efficient version of the method uses ray tracing or beam tracing for searching the valid image sources. The restriction of the image source method is that it can not model edge diffraction or diffuse reflections.

The lack of modelling of edge diffraction generally creates unphysical discontinuities in the modelled sound field. This creates anomalous situations in which reflections can suddenly appear or disappear when the receiver position changes. The addition of secondary edge sources can rectify these discontinuities [22]. The edges are subdivided into edge elements that are secondary sources with a specified directivity function. Like the image sources, also the edge sources require visibility checks.

Ray tracing

Ray tracing [23] [1] is another method for computing the paths of specular reflections. Instead of finding the specular reflections exactly, a multitude of closely spaced sound particles, carrying equal energy, are sent out and reflected upon contact with walls. Because the modelled quantity is the sound energy, any phase effects are neglected. The $1/r^2$ distance attenuation of spherical spreading is provided inherently in the method by the growing distance between adjacent rays. The ray energy may furthermore be attenuated by air absorption and surface absorption. A ray is traced until its energy falls below a threshold value that characterizes it as negligible.

The receiver is modelled as a volume and intersection tests have to be done to determine which rays contribute to the response at the receiver. The method can be modified by using beams or cones instead of rays, which then allows the use of point receivers instead of volumes. In contrast with the image source method, ray tracing can handle diffuse reflections by introducing scattering coefficients for the surfaces. Upon contact with a wall, a random number is generated and if it falls

below the value of the scattering coefficient, the reflection is treated as diffuse. Due to the amount of rays being limited, some reflection paths may be missed by the method. Similarly to the image source method, the restriction of ray tracing is that edge diffraction can not be modeled and the generated sound field will therefore often suffer from discontinuities.

Radiosity method

The acoustic radiosity method [24] is a geometric method for modelling diffuse reflections. The method is similar in principle to ray tracing but instead of sending out a large amount of rays, the boundaries are divided into smaller surface elements that radiate rays between each other. Similarly to ray tracing, the method is based on energies rather than pressures and is thus an incoherent method incapable of modelling interference effects. The surfaces are assumed to be diffusely reflecting, and to follow Lambert's law [1]. Therefore the direction of reflection is independent of the direction of arrival which allows simplifications in the model development. The form factors, i.e. the contribution strengths between each pair of two elements, are calculated separately for all element-to-element combinations. The incident sound intensity on one element can then be described in terms of a sum of contributions from the source and all the other elements.

The ART method is a similar method in principle to the radiosity method but instead of being limited by the assumption of Lambertian diffuse reflections, the method can model arbitrary directional patterns [25]. Thus the method presents a step towards more realistic modelling of reflections.

2.3.2 Wave-based methods

In contrast to the geometric methods, the wave-based methods aim at a direct numerical solution of the wave equation. Thus the effects that are inherent for waves, interference and diffraction, are automatically included and do not need any special consideration. It would therefore at first glance seem preferable to avoid the geometric methods altogether and instead use the wave-based methods for all purposes. However, the computational demands for these methods grow very rapidly with increasing bandwidth. In practice, the usability of the wave-based methods is often limited to the low and mid frequencies. In the following, a few of the common wave-based acoustic modelling methods are discussed.

Finite-difference time-domain method

In the finite-difference time-domain (FDTD) method for acoustic modelling [26] [27], the modelled space is discretized by forming a uniformly spaced and shaped mesh. The topology of the mesh can take several different forms. The second-order partial derivatives of the wave-equation are approximated with finite differences and the total sound field is computed in a time iterative manner. A relative of the FDTD methods is the family of digital waveguide mesh (DWM) [28] methods, of which the methods with similar stencils are mathematically equivalent [29]. The 3-D SRL

FDTD method is explored in more detail in Section 3.

Finite element method

The finite element method (FEM) [30] divides the volume of the modelled space into small elements of arbitrary shape and size. The sound field inside each element is forced to fulfil the wave equation in an average sense and the pressure is forced to be continuous along the surface of the element. Given an initial state of the system, the total sound field can be computed in the frequency domain for point frequencies. Alternatively, the sound field can be solved in a time iterative manner using a finite-difference scheme. The FEM and FDTD have a degree of similarity and the FDTD method can be seen as a special case of the FEM. FEM is more accurate compared to the simpler FDTD method, but computationally more demanding due to the involved precalculation procedures. Also, the FEM has the advantage over the FDTD method of being able to fit non-axis aligned walls without staircase approximation because of the possibility of using non-uniform element shapes.

Boundary element method

The Helmholtz-Kirchoff integral describes the pressure at a point as a sum of the pressure from the source(s) and a surface integral of the pressure and its derivative over the reflecting surfaces [7]. The boundary element method (BEM) presents a numerical solution to this integral in the frequency domain. The boundary surface is divided into elements that generally need to be smaller than 1/8 of the wavelength for the results to be considered valid. The first step in BEM is to calculate for the surface elements the source signals that fulfil the boundary conditions of the space. The second step is the integral calculation, where the sum contribution from all the surface elements to an external point is computed. It is possible to either solve the sound field separately for point frequencies in the frequency domain, or use time-domain formulations to calculate the impulse response. The advantage of BEM over the volumetric methods is that open space does not need modelling.

Adaptive rectangular decomposition

The adaptive rectangular decomposition (ARD) [31] method is an efficient and dispersion-free alternative to the FDTD methods. An optimized parallel implementation of ARD on a GPU has been shown to perform up to three orders of magnitude faster than prior techniques based on FDTD [32]. The method exploits the fact that the analytic solution for the wave equation is known for rectangular domains. After the meshing, the space is decomposed into rectangular subdomains. The solution to the wave equation in the subdomains can then be expressed in terms of the discrete cosine transform (DCT). The DCT can be efficiently calculated through FFT and the pressure values for each time step are obtained through the inverse DCT. Interfacing between the subdomains introduces a small error manifested as low amplitude reflections that emanate from the interface boundary. However, the errors are below the level of audibility and thus the method is promising for auralization purposes.

3 The Finite-Difference Time-Domain method

This section presents a brief introduction to the finite-difference time-domain (FDTD) method for room acoustic simulation by introducing the basics of the 3-D standard rectilinear (SRL) method. In this thesis, both the 2-D and 3-D SRL methods are explored but here only the 3-D method is discussed as the derivation of the 2-D method is analogous in nature.

3.1 Introduction

FDTD is a method for approximating wave propagation in isotropic media in one or more dimensions. The method originated in the electromagnetics field [33] and was later adapted to acoustics. The principle is to discretize the second order spatial and temporal partial derivatives of the wave equation by approximating them with second order central finite differences. The accuracy of the modeled wave phenomena then depends on how fine or coarse the discretization is.

The FDTD method has been successfully applied to a variety of problems in acoustics. In [34] and [35], the 1-D method was applied to the modelling of brass instruments. In [36] and [37], the 2-D method was used to study diffusers, their time spreading and obtainment of the diffusion and scattering coefficients. The 3-D FDTD method has been used e.g. to study the well-known seat-dip effect [38] [39] and for accompanying the beam-tracing method in studying the acoustics of the Epidaurus theatre [40].

The time-iterative nature of the FDTD method lends itself naturally to the production of visualizations of sound propagation. The use of visualizations allows for a more intuitive grasp of complicated phenomena in studies of wave propagation. An example of this was shown in [41], where the 2-D FDTD method was successfully applied to the visualization of sound propagation around noise barriers and semi-underground road structures.

FDTD is computationally very intensive for high frequency applications. As an example, suppose that a doubling of the sampling frequency is needed for a 3-D FDTD simulation. The internodal distance is then halved and in all three dimensions double the amount of nodes is needed to represent the same space. In the time domain, double the amount of samples is needed to represent the equivalent time span. Thus, the memory requirements grow $2^3 = 8$ fold and the amount of required computation is then $2^4 = 16$ fold.

In practice, the hefty computational requirements limit most simulations to offline computation. Also, the acoustic space size is often limited to a medium sized room and the usable bandwidth well below the upper limit of human hearing, even in offline simulations. At present it is generally not feasible to approximate free-field conditions in 3-D simulations merely by enlargening the simulation space. For 2-D simulations, however, approximating free field conditions by enlargening the simulation space is feasible in some situations. For simulation of low- and mid-frequencies, real-time processing is possible using a graphics processing unit (GPU) for the computation tasks, as was shown in [42].

A well known problem in FDTD room simulations is that it is difficult to approximate anechoic conditions. Consequently, there have been efforts directed at circumventing the limitations imposed by this. For instance, a perfectly matched layer (PML) medium suitable for acoustic wave propagation has been derived in [43]. Near to far field transformation can also be used to approximate the response of a scattering surface in the far field when only limited space is available [7].

3.2 Discretization of the 3-D wave equation

In 3-D isotropic space, sound wave propagation is governed by the wave equation [1], which can be written in the cartesian coordinate system as

$$\frac{\partial^2 p}{\partial t^2} = c^2 \left(\frac{\partial^2 p}{\partial x^2} + \frac{\partial^2 p}{\partial y^2} + \frac{\partial^2 p}{\partial z^2} \right) , \tag{3.1}$$

where t is the time variable, p is the acoustic sound pressure and c is the speed of sound. For a numerical solution method, the second-order partial derivatives can be approximated with finite differences [44]. The discretized wave equation is then

$$\frac{p_{i,j,k}^{n+1} - 2p_{i,j,k}^{n} + p_{i,j,k}^{n-1}}{T^2} = c^2 \left[\frac{p_{i+1,j,k}^{n} - 2p_{i,j,k}^{n} + p_{i-1,j,k}^{n}}{X^2} \right.$$
$$+ \frac{p_{i,j+1,k}^{n} - 2p_{i,j,k}^{n} + p_{i,j-1,k}^{n}}{X^2}$$
$$\left. + \frac{p_{i,j,k+1}^{n} - 2p_{i,j,k}^{n} + p_{i,j,k-1}^{n}}{X^2} \right] , \tag{3.2}$$

where T is the time step, X is the spatial step, $p_{i,j,k}^{n}$ is the update variable, n is the time index, and i, j and k denote the indices for spatial directions x, y and z, respectively. Solving equation (3.2) for the pressure value at future time index $n+1$ gives the 3-D FDTD update equation for a rectilinear topology:

$$p_{i,j,k}^{n+1} = \lambda^2 \left[p_{i+1,j,k}^{n} + p_{i-1,j,k}^{n} + p_{i,j+1,k}^{n} + p_{i,j-1,k}^{n} + p_{i,j,k+1}^{n} + p_{i,j,k-1}^{n} - 6p_{i,j,k}^{n} \right]$$
$$+ 2p_{i,j,k}^{n} - p_{i,j,k}^{n-1} , \tag{3.3}$$

where $\lambda = cT/X$ is called the Courant number. For the 3-D SRL FDTD scheme [29], a value of $\lambda = \sqrt{1/3}$ is used, which is also the upper limit of stability, and gives

$$p_{i,j,k}^{n+1} = \frac{1}{3} \left[p_{i+1,j,k}^{n} + p_{i-1,j,k}^{n} + p_{i,j+1,k}^{n} + p_{i,j-1,k}^{n} + p_{i,j,k+1}^{n} + p_{i,j,k-1}^{n} \right] - p_{i,j,k}^{n-1} \tag{3.4}$$

as the update equation. The grid spacing – i.e. the distance between any two adjacent sampling points or 'nodes' in the mesh – is

$$X = \frac{c}{f_s \lambda} , \tag{3.5}$$

where $f_s = 1/T$ is the sampling frequency of the system. The process of translating a 2-D or 3-D geometry from sets of polygons to a discrete set of interconnected air nodes and boundary nodes is referred to as meshing.

3.3   Boundaries

In the 3-D SRL FDTD scheme, every air node has six neighbours. For boundaries, however, there are special cases to consider where one, two or three of the neighbouring nodes may not exist. These are so called 'ghost nodes' that need to be addressed in the boundary update equations by applying the appropriate boundary conditions. Figure 3.1 shows the different types of neighbour configurations that can be found in a SRL topology for a basic shoebox-type space.
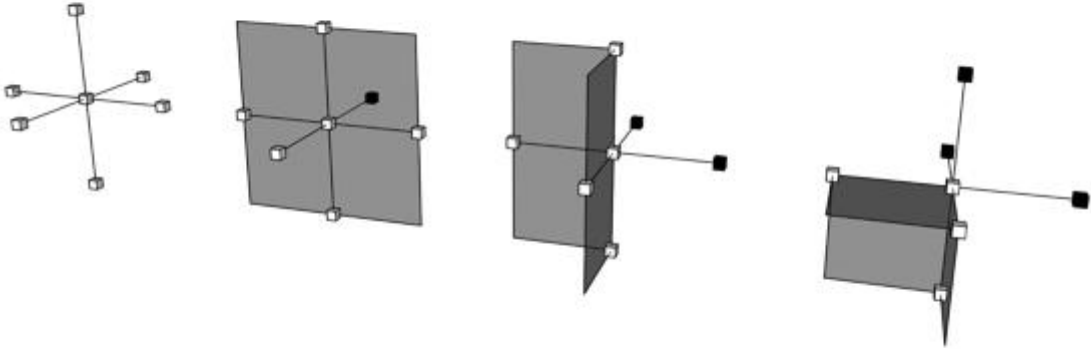

Figure 3.1: The 3-D SRL FDTD neighbour configurations. From left to right: air, plane, outer edge, outer corner. White cubes denote mesh nodes and black cubes denote ghost nodes. The grey surface represents the space boundary.

The neighbourhoods shown for the edge and corner are of the outer type, i.e. they feature ghost nodes (denoted as black cubes in the figure). For inner edges and corners there are no ghost nodes and the general update equation (3.3) is valid as it stands. For a plane boundary, one of the neighbour nodes is always lying outside the simulation space. Similarly for an outer edge, two of the neighbour nodes are outside the space and for an outer corner, three nodes are outside. In total there are 26 possible neighbourhood configurations at boundaries for different boundary orientations; 6 for plane boundaries, 12 for edges and 8 for corners.

At the boundaries, both the wave equation and boundary conditions must apply simultaneously. In case one or more of the neighbour nodes do not exist, the ghost nodes need to be eliminated from the update equation by applying the appropriate boundary conditions, i.e. one condition for each axial direction that has a ghost node. As an example, the boundary update equation for a right boundary is derived. The boundary is assumed to be locally reacting (see Section 2.2.1). The appropriate boundary condition for a right boundary of this type is [29]

$$\frac{\partial p}{\partial t} = -c\xi_w \frac{\partial p}{\partial x} \ , \tag{3.6}$$

where ξ_w is the specific wall impedance. Approximating the partial derivatives with finite differences gives

$$\frac{p_{i,j,k}^{n+1} - p_{i,j,k}^{n-1}}{2T} = -c\xi_w \frac{p_{i+1,j,k}^{n} - p_{i-1,j,k}^{n}}{2X} \ . \tag{3.7}$$
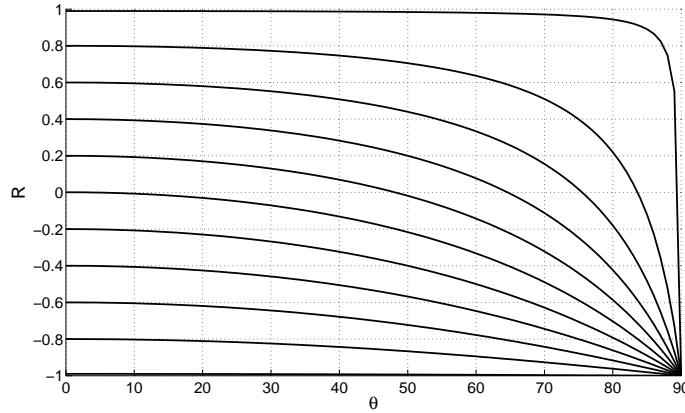
Figure 3.2: Expected reflectance values for various reflection coefficient values and azimuth angles (elevation at $0°$).

Solving for the pressure value at the ghost point yields

$$p_{i+1,j,k}^n = p_{i-1,j,k}^n - \frac{1}{\xi_w \lambda}(p_{i,j,k}^{n+1} - p_{i,j,k}^{n-1}) \ . \tag{3.8}$$

Next, this result is substituted for the ghost point in equation (3.3), which gives the appropriate update equation for a right boundary as

$$
\begin{aligned}
p_{i,j,k}^{n+1} &= \Big[\lambda^2\Big(2p_{i-1,j,k}^n + p_{i,j+1,k}^n + p_{i,j-1,k}^n + p_{i,j,k+1}^n + p_{i,j,k-1}^n - 6p_{i,j,k}^n\Big) \\
&+ 2p_{i,j,k}^n + \Big(\frac{1}{\xi_w \lambda} - 1\Big)p_{i,j,k}^{n-1}\Big]/\Big(1 + \frac{1}{\xi_w \lambda}\Big) \ .
\end{aligned}
\tag{3.9}
$$

For the other boundary types, a similar method of substitution for each ghost point in the update equation must be used. A more thorough discussion about the subject can be found in [29]. The plane-wave reflection coefficient for a 3-D locally reacting boundary can be obtained by extending equation (2.26) to 3-D [29]:

$$R(\theta, \phi) = \frac{\xi_w \cos\theta \cos\phi - 1}{\xi_w \cos\theta \cos\phi + 1} \ , \tag{3.10}$$

where θ and ϕ are the azimuth and elevation angles, respectively, signifying deviation from the surface normal. In addition to the assumption of locally reacting boundaries, the reflection coefficients for the employed FDTD methods are frequency-independent. Solving from equation (3.10) the specific wall impedance for a plane-wave of normal incidence (i.e. $\theta = 0°, \phi = 0°$) gives

$$\xi_w = \frac{1 + R(0,0)}{1 - R(0,0)} \ . \tag{3.11}$$

The expected reflectances for all angles of incidence can be obtained by assigning the boundary reflection coefficient to equation (3.11), using the obtained specific impedance in equation (3.10) and solving for angles $0° \ldots 90°$ for θ and ϕ. Expected reflectance values for various azimuth angles ($0°$ elevation) are given in Figure 3.2.

4 Simulation preliminaries

The aim of the simulations is to examine the effect of surface structures on the reflected sound. Taking into account the limitations of FDTD and the objective of the thesis – which is to study surface reflection characteristics in regard of structural parameters – designing the simulation setup to facilitate meaningful and good quality results requires careful consideration. This section deals with the issues related to the simulation setup design by discussing relevant matters (e.g. source and receiver positioning), exploring the FDTD methods by means of introductory simulations, and comparing the 2-D and 3-D simulations of a wall structure.

It is shown that the 2-D FDTD is a better choice for the main work of this thesis. The end result of this section is an approach that is followed in the main body of simulations presented in Section 5.

4.1 Simulation setup and processing of results

It is preferable to have the source and receivers situated in a way that allows for a sufficiently long propagation path for the sound, so that a sufficient approximation for a plane wave is obtained. In order to monitor both the near and far fields, it is also advantageous to be able to place receivers simultaneously at many positions at different distances from the object. For low frequency resolution, it is crucial to have a long enough time window of sample material available. As the software used for the FDTD simulations is limited to locally reacting boundaries with frequency-independent reflection coefficients – which can not be made properly absorptive for a full range of incidence angles as seen in Figure 3.2 – the simulation space boundaries must be positioned further away to ensure that no extraneous reflections arrive at receivers within the target time window. These criteria are somewhat attainable in 2-D when due consideration is exercised, but they present more of a challenge in 3-D because of the inherently larger computational demands.

In measurements, the direct sound is often blended with the reflected sound. Sometimes the object of investigation is the total sound at receivers, if for example the comb filtering effect of the combination of direct and reflected sound is to be studied. However, for the purposes of this thesis, it is the nature of the reflections that is of primary interest and thus the direct sound only presents a hindrance. For some cases, it is possible to situate the source and receivers in such a way as to allow for simple time gating to isolate the reflections. Another method that leaves more flexibility – in terms of choice of source/receiver positions – is to also obtain the direct sound at receivers in isolation. The reflections can then be separated by subtracting the direct sound from the results [45].

In real world measurements, the clean subtraction of direct sound presents a challenge due to differences in the fine details of the responses. The differences are caused by unavoidable small discrepancies in the setup (i.e. source and receiver positions) and the surrounding medium between sessions due to varying temperature, humidity etc. Fortunately, in the simulation environment it is possible to replicate the measurement setup exactly and as a result the direct sound can be perfectly

removed from the results. Figure 4.1 illustrates the application of the subtraction principle to an example simulation result. All the reflection studies conducted for this thesis utilize this subtraction procedure.
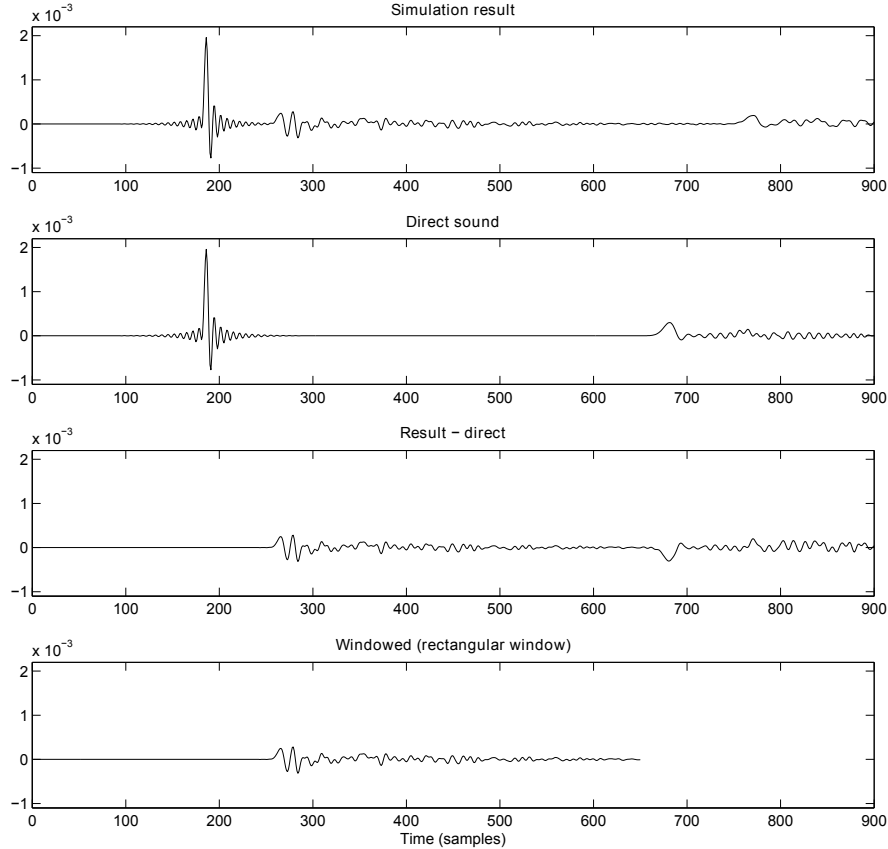

Figure 4.1: The isolation of reflected sound from a receiver response. The responses are from 3-D simulations.

All the models for the main simulations are meshed in a way, whether in 2-D or 3-D, that gives approximately 1 cm as the internodal distance (see equation (3.5)), unless stated otherwise. For the 2-D method, the sampling frequency is therefore 48,6 kHz and for 3-D it is 59,6 kHz. This ensures a high degree of comparability between models and predictability in the translation process from the models to meshes. A sufficiently wide frequency band for which the results can be considered valid is also obtained. The receiver impulse responses are filtered with a lowpass filter in order to get rid of aliasing effects and to reduce the observed bandwidth to a reasonably accurate (in terms of dispersion) domain. However, the very high frequencies, beyond about 3–4 kHz, are not the primary focus of the investigation so in general less attention has to be paid to eliminating the high frequency dispersion phenomenon. After subtraction, to remove any unwanted reflections, the responses were windowed with a vector of ones concatenated with the latter half of a Hann window. This ensured that the windowed responses reach zero to avoid windowing artifacts. After the windowing, fast Fourier transforms (FFT) were computed for

the responses.

Figure 4.2 a) shows an example case of magnitude responses of reflections obtained for a line of receivers. The main characteristics of the responses are roughly the same for the line of receivers up to about 2 kHz. The higher frequencies vary more due to the scattering effects becoming prominent. At these frequencies the responses have such a large degree of randomness that it is impossible to draw any conclusions by looking at them in this manner. In light of these observations, an obvious improvement is to use the average of the magnitude responses for analysis instead. Figure 4.2 b) shows the averaged response for the same results. The common characteristics of the responses – the notches under 2 kHz – are retained and the randomness of the high frequencies is smoothed out to give a more general sense of what is happening in the reflection. Also, the comb filtering effect becomes more obvious in the averaged response. It is quite evident that this is a more meaningful way to view the results. Therefore, the frequency responses from various simulation cases were generally averaged over a range of receiver positions and then converted to sound pressure levels in the dB scale.
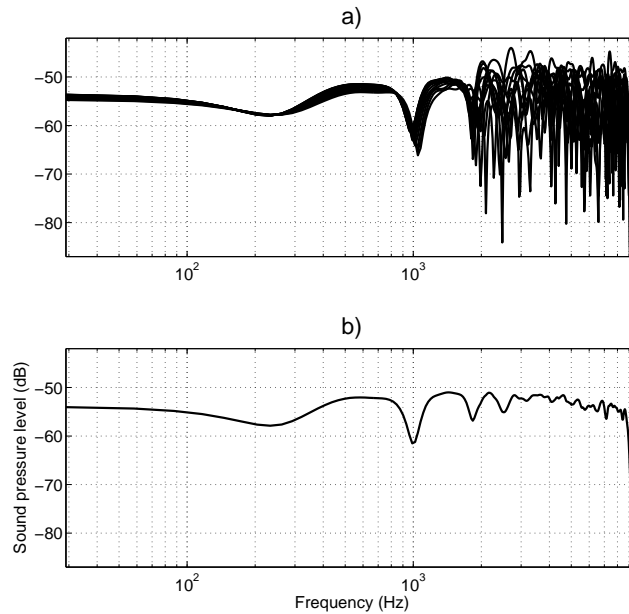

Figure 4.2: a) individual magnitude responses for a line of 12 receivers, b) the average magnitude response.

4.2 Introductory simulations

This section presents simulations that serve as a means of better understanding, validating the method and developing the specific post-processing steps taken in analyzing the results. The idea is that if the results match the characteristics of the methods, as represented by analytical solutions and common qualitative under-

standing, it is taken to mean that the specific method used here is working properly and the post-processing steps involved are valid.

4.2.1 Dispersion

A characteristic of the rectilinear FDTD methods is the frequency- and direction-dependent dispersion. In other words, the wavefronts travel at different speeds depending on the frequency and the direction of travel. The higher the frequency, the stronger the dispersion effect. For the SRL method, the dispersion effect is worst for the axial directions and non-existent for the diagonal directions. The theoretical limits for the valid frequency ranges of the 3-D and 2-D SRL FDTD methods are $0.196 \times f_s$ and $0.25 \times f_s$, respectively [46]. Thus a very high sampling frequency is needed in order to ensure valid results at a wide range of audible frequencies.

Simulations of free field propagation were performed to explore the dispersion in 2-D and 3-D. For 3-D, a rectangular space of 360 x 330 x 360 nodes was used. For the axial propagation case, a source and a receiver was positioned at the middle points of the x- and z-axes, at distances of 80 and 250, respectively, from the y = 0 boundary. The model and source/receiver geometry ensure that the direct sound and the boundary reflections are not overlapped and therefore the direct sound can be cleanly isolated. The simulations were done separately for the axial, side-diagonal and diagonal propagation directions.

The model space was appropriately rotated for the side-diagonal and diagonal cases before meshing so that the same relative arrangement for the model space and source/receiver positions could be used and thus all three cases would yield directly comparable results. The distance that the sound impulse traverses from source to receiver is 170 internodal distances. The results were filtered with a linear-phase lowpass filter with cutoff frequency at $0.17 \times f_s$. Figure 4.3 shows the results for all three cases. The axial and side-diagonal propagation directions exhibit clearly identifiable dispersion effects, the axial direction being the worst. The 3-D diagonal direction, however, is free of dispersion.

Figure 4.4 presents the equivalent results from a 2-D simulation where the direct impulse was recorded at axial and diagonal directions at 170 internodal distances away from the source position. Similarly to the 3-D dispersion test, the space was made large enough to ensure clean obtainment of only the direct sound at receivers. Because of the lower computational requirements of the 2-D simulation compared to 3-D, clean responses for both propagation directions could be comfortably obtained within the same simulation. As before, the effect of dispersion is readily seen in the axial direction response whereas the 2-D diagonal direction is free of dispersion. In Figure 4.4b the spectrograms of the results show another peculiar effect that is manifested as low frequency energy that persists for some time after the initial impulse has passed. This is the *afterglow* effect [47] that is characteristic of the 2-D FDTD method.
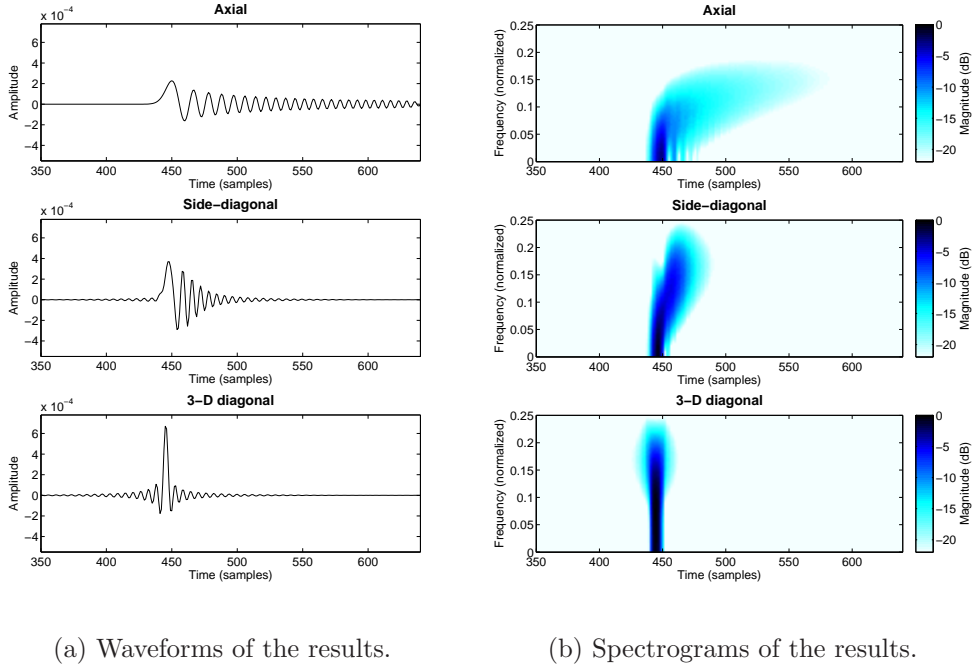
(a) Waveforms of the results.　　　(b) Spectrograms of the results.

Figure 4.3: 3-D dispersion: axial (top), side-diagonal (middle) and diagonal (bottom) propagation directions.

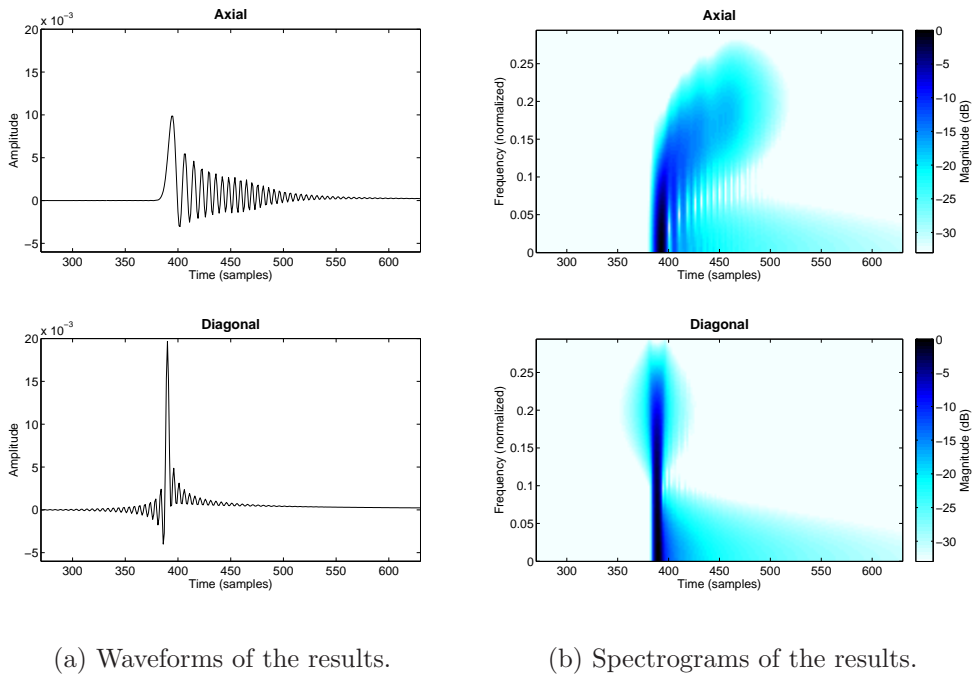(a) Waveforms of the results.　　　(b) Spectrograms of the results.

Figure 4.4: 2-D dispersion: axial (top) and diagonal (bottom) propagation directions.

4.2.2 Boundary reflectance

The boundary reflectance provides a good subject for study because of the readily available comparison with the analytical solution. Therefore it can serve as a calibration/validation tool for the method and the post-processing steps. Figure 4.5 shows a snapshot of the arrangement for studying the reflectance for different reflection angles in 2-D FDTD. The source is situated at 1.5 meters and the receiver line at 0.5 meters from the reflecting wall. The receiver positions were chosen to give the responses at angles 0° to 85°, in 1° increments. The 0° angle is the reflection direction normal to the surface. The geometry of the model space and the source/receiver positions were designed to allow for the wall reflections to arrive and pass before any reflections arrive from the boundaries of the simulation space.
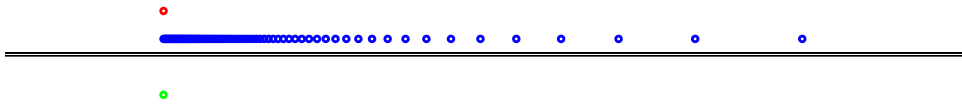
Figure 4.5: Snapshot of the source/receiver setup with respect to the position of the reflecting surface; red circle = source, green circle = image source, blue circle = receiver.

The simulation was separately run for each studied reflection coefficient value. In addition, two simulations were run with the reflecting surface removed to obtain the direct sound and models for ideal reflections. The ideal reflections were obtained by removing the original source and replacing it with an image source that was mirrored with respect to the position of the removed surface. In this way the path length attenuation is equivalent for the reflections and the corresponding ideal reflections. All the responses were filtered with a lowpass filter with cutoff at $0.15 \times f_s$. In addition, a DC-block filter was used to try to eliminate the accumulating bias inherent in the FDTD simulation. Starting points of the ideal reflections were detected for all the receivers and a tapered window was accordingly positioned to separate each response.

The direct sound was subtracted from all the responses and the individual reflection response energies were obtained through squaring and summing the sample values. The value of the reflectance was then given by the square root of the ratio of the result and image source energies. As the ratio represents only the absolute value of the reflectance, the results had to be manually rectified for phase shifts that exceed $\pi/2$ by changing the sign of the result whenever the corresponding expected value was negative. Figure 4.6 shows the results for the simulated and expected reflectance values. Generally the results follow the expected values closely. However, whenever the expected reflectance approaches zero, the simulated results are 'deflected' away, i.e. the ratio of the energies can not reach below a certain point. The effect is due to either DC offset or the afterglow effect that biases the energy ratios.
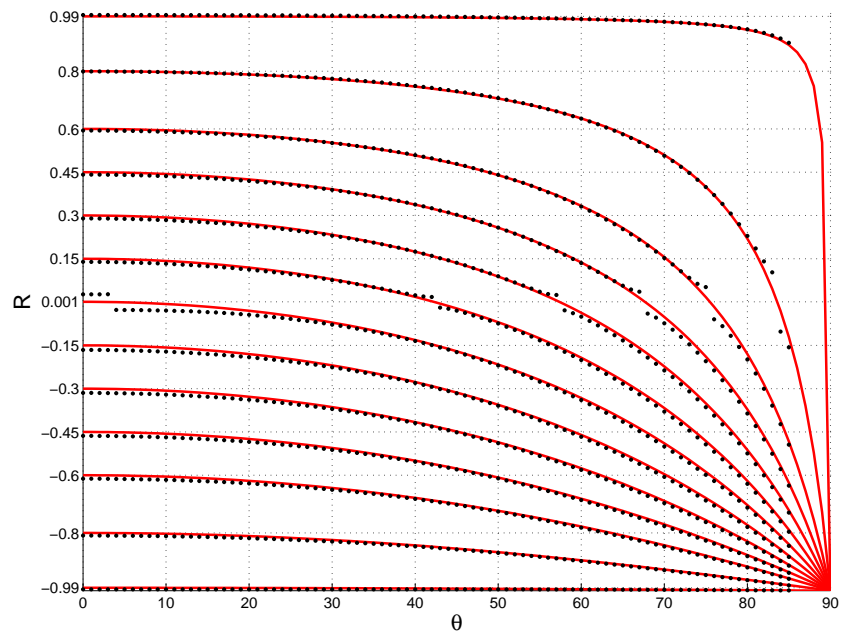
Figure 4.6: Expected and simulated reflectance for various angles for the reflection coefficient values shown in the figure; red (solid line) = expected, black (dots) = simulated; the simulated angles are $0° \ldots 85°$, in $1°$ increments
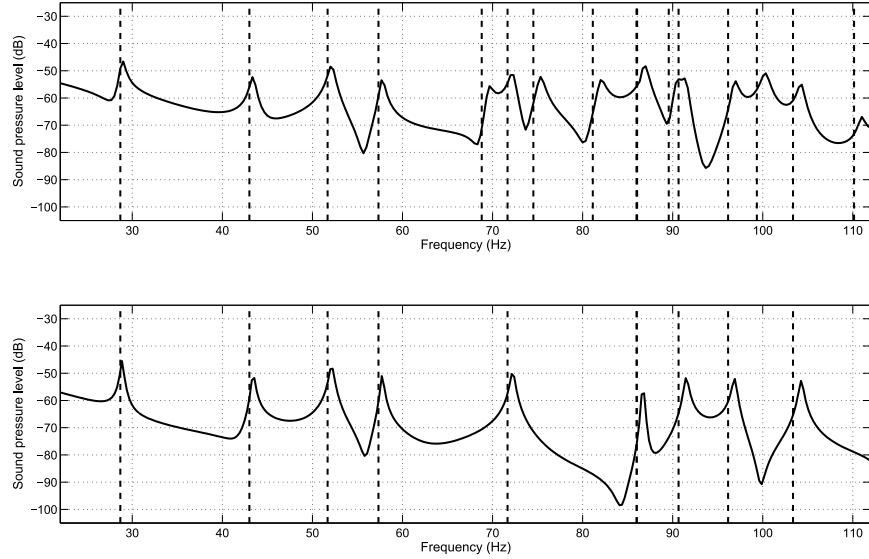
Figure 4.7: First 15 modes of the room as represented by the 3-D (top) and 2-D (bottom) results. The vertical dashed lines show the predicted values for the modal frequencies.

4.2.3 Modes in a rectangular enclosure

The modes of a rectangular enclosure is one of the rare cases for which a full analytical solution is available. A direct comparison with simulation results is therefore possible. Investigation of room modes in the form of 2-D and 3-D simulations were done for a rectangular room with hard walls. The expected modal frequencies are given by [10]

$$f_{n_x n_y n_z} = \frac{c}{2} \left[\left(\frac{n_x}{L_x} \right)^2 + \left(\frac{n_y}{L_y} \right)^2 + \left(\frac{n_z}{L_z} \right)^2 \right]^{1/2} , \tag{4.1}$$

where $n_x, n_y, n_z = 0, 1, 2, \ldots$ and L_x, L_y, L_z are the dimensions of the room. The expected modes for the 2-D simulation are a subset of the modes for the whole 3-D room and only include the axial and tangential modes of the xy-plane. A 3-D room model of dimensions 4 m × 6 m × 2.5 m was made for the purpose of the simulations. In the 3-D case, the whole room was meshed whereas in the 2-D case, a 4 m × 6 m xy-slice of the room was meshed.

A source and a receiver was positioned near the opposite corners of the same xy-slice in both cases. Sampling rates of 20000 Hz and 16330 Hz were chosen for the 3-D and 2-D simulations, respectively. This results in equal internodal distances for both cases and the sampling frequencies are high enough to ensure that the studied modes are unaffected by dispersion. The simulations were run for approximately three seconds for both cases in order to let the room modes build up sufficiently for detection. Figure 4.7 shows the results along with the predicted modal frequencies for the first 15 modes of the room. It can be seen that the results are in good agreement and follow the predicted values closely. The small misalignment of the higher modes is caused by the dimensions of the room being slightly shorter than

intended due to the limited accuracy inherent in the meshing.

4.3   3-D vs 2-D

Ideally, FDTD simulations pertaining to room acoustics should be conducted in 3-D because it represents a more faithful reproduction of the acoustical phenomena, for obvious reasons. However, due to the severe limitations imposed by the computational requirements of a full 3-D simulation, 2-D simulations have to be used instead, for some cases. Fortunately, the results from 2-D and 3-D simulations can be equivalent in some situations, disregarding the afterglow effect [47] that is inherent in the 2-D FDTD but non-existent in 3-D. In the following, the potential equivalence of results from the 2-D and 3-D SRL FDTD methods is explored. Furthermore, the effect of response length and path length is shown to justify the simulation setup that is developed.

4.4   Slatted panel structure with a flat back wall
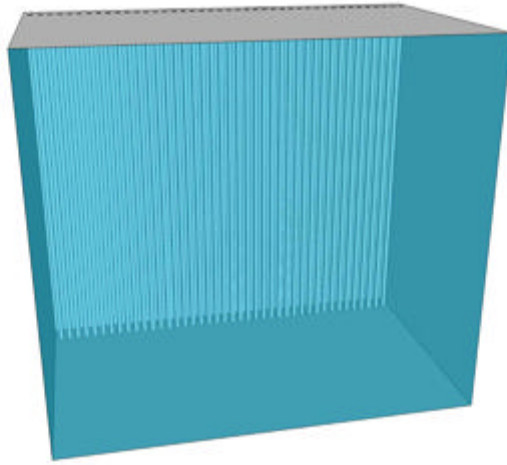
Figure 4.8: The 3-D model for the simulation. The object of investigation is the 5 cm × 5 cm slatted panel with 50 % open area and the flat back wall behind it.

Figure 4.8 shows the full 3-D model used for the simulations. The simulation space was designed so that no extra reflections from boundaries above, below and at sides would reach the receivers within a target time window. This was ensured with the help of a beam tracing algorithm [48] by investigating the arrival times of first reflections for each receiver position. The object of investigation is the structure consisting of a 5 cm × 5 cm slatted panel with 50 % open area, and a flat back wall behind it. The space between the slatted panel and the back wall forms a 20 cm deep cavity. The structure is in principle similar to the *distributed Helmholtz resonator* structure presented in Section 2.1.6, but the design parameter range is different. Typical resonant absorbers of this form have panels with considerably less

open space and also include absorbing material inside the cavity to provide a loss
mechanism that converts acoustic energy to heat.

For the 2-D simulation, the model was extended to the directions of the side
walls while keeping the dimensions of the studied structure the same. The extension
was done in order to allow for greater response lengths and also the option of longer
distances for source and receivers. As in the 3-D simulation, no extraneous reflections
were allowed in the 2-D simulation. To minimize the effect of edge diffraction from
the transition point between the studied structure and the front wall, a reflection
coefficient of 0.001 was applied to the front wall and the corners between it and the
studied structure. A reflection coefficient of 0.95 was applied to the structure itself.

A peculiar side-effect of the 2-D FDTD method that is not present in 3-D is
the *afterglow* effect [47], shown in Figure 4.4, which is a direct consequence of the
wave equation in even dimensions. The effect manifests itself in that after the initial
passing of a wavefront at a receiver point, the sound pressure will not go to zero,
but rather tend towards it asymptotically. The result of this is a filtering effect,
which makes the frequency response of an impulse slope-like in the way that the low
frequencies are emphasized. Equalization of the afterglow effect in 2-D simulations
for propagation in free space was shown in [47]. However, equalization for a more
practical case with reflections from boundaries is yet to be developed. For this
reason, a practical method of compensation was applied to the 2-D results in this
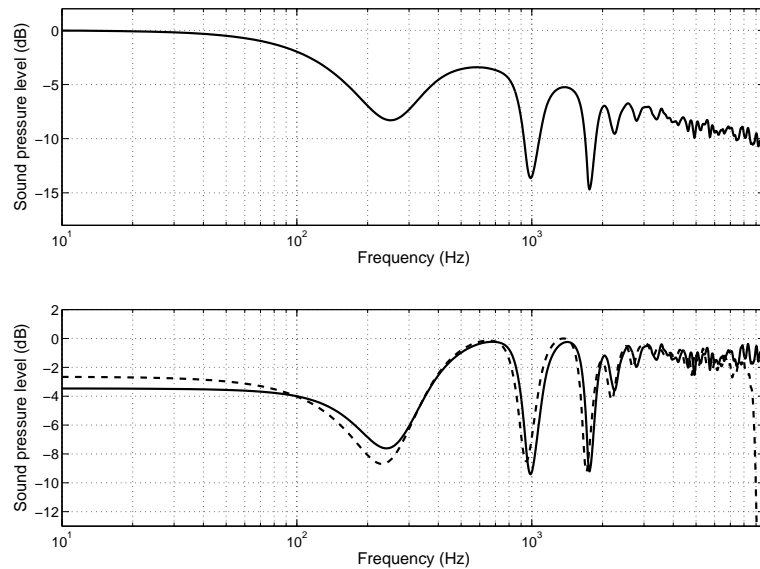thesis by normalizing the results with respect to a flat wall response.

Figure 4.9: Top: the 2-D result, showing the afterglow effect; bottom: the compen-
sated 2-D result (solid line) with the equivalent result from a 3-D simulation (dashed
line).

The top graph in Figure 4.9 shows the result (average frequency response for a line of receivers) for a 2-D slice of the model shown in Figure 4.8. The effect of the afterglow is seen in the slope-like tendency of the response. The bottom figure shows the same result with compensation applied, and compared to an equivalent 3-D simulation result, with similar length windowing with respect to time. The source is at 60 cm from the panel and a line of 20 receivers is at 30 cm from the panel. It is seen that the 2-D and 3-D results are qualitatively similar, exhibiting similar features in the responses. The higher frequencies show more deviation due to the different dispersion characteristics of the 2-D and 3-D methods.

4.4.1 Window length and receiver distance effects

While the reflection-free response length used for obtaining the results in Figure 4.9 is at the limits of the available resources for the 3-D method, the 2-D method enables lengthier responses. Figure 4.10 demonstrates how the mean frequency response obtained from the 2-D simulation changes when longer windows are used. In this case, the windows are not normalized to starting points of the reflection impulses, and thus the relative length instead of the absolute length of the responses is of interest here. The frequencies of the three notches between 250 Hz and 2 kHz in the responses are identified correctly even with the shortest window. However, their effect is overemphasized as can be seen by comparing the results against the responses with longer windows. In addition, one more notch at 100 Hz is not found until the window size is almost doubled. Even with the longest window, it remains doubtful whether the frequencies below 100 Hz can be considered valid because the longest response is still quite short with regard to the very low frequencies.
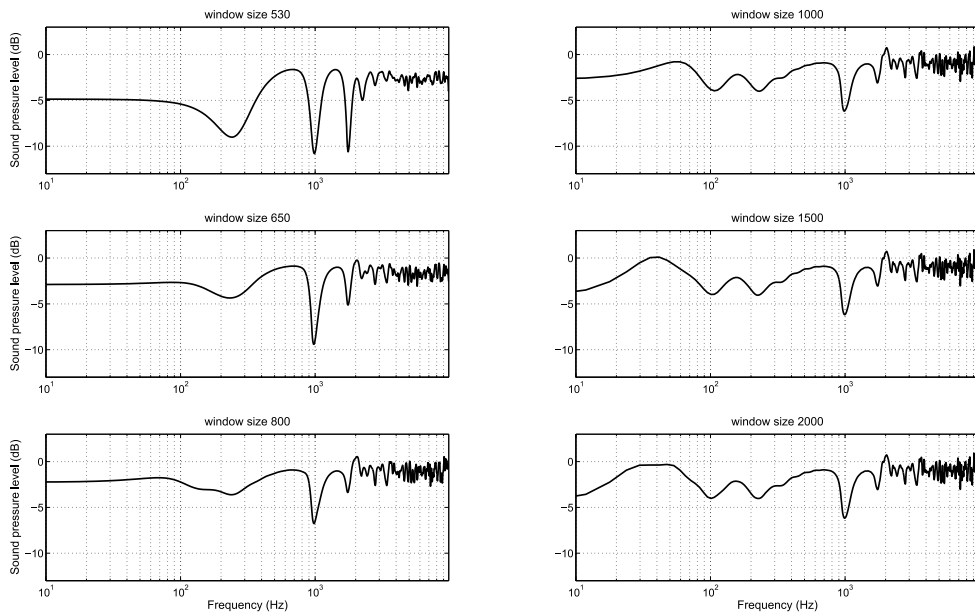

Figure 4.10: The effect of window (response) length on the mean frequency responses. 1000 samples corresponds to about 21 milliseconds.

Figure 4.11 demonstrates the effects of receiver distance on the frequency responses by presenting averages from 20 receivers at different distances from the slatted panel structure. The first line corresponds to the case shown in Figure 4.10 and the other lines of receivers are always one meter further away from the panel, i.e. the last line of receivers is at a distance exceeding five meters. The source is kept at the same position as before. The responses are windowed with windows whose starting points are normalized for each line of receivers. A long tapering (3/4 of the window length) is used for the window by utilizing a half Hann window. This is done in order that the 2-D reference flat wall responses have valid low frequency responses. Otherwise the reference responses would be distorted because the truncation and the afterglow effect combine to make the low frequency response non-flat. The compensated results would then be rendered invalid.
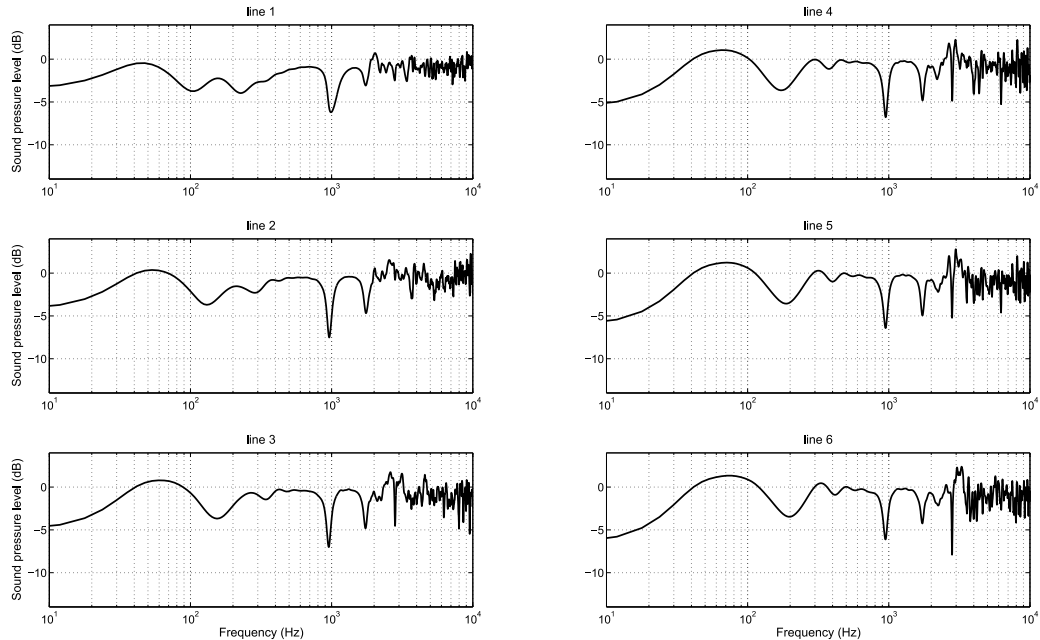

Figure 4.11: The effect of distance on the mean frequency responses.

The low frequency notches that are originally (line 1) at about 100 Hz and 200 Hz, drift upwards as the distance from the panel grows. The notches are probably produced by interference from diffracted waves from the slat edges, and thus the frequency drifts upwards as the path length difference between the direct reflection path and the diffracted waves diminish as the distance from the object grows. The notches between about 900 Hz and 1800 Hz, however, can be found in every result at nearly the same frequencies and it seems therefore that these are a result of a more general effect of the structure, presumably caused by the cavity depth. A new feature that becomes apparent from line 3 responses onwards is the highly concentrated high frequency notch at slightly below 3 kHz.

In Section 2.1.2 the near field and far field was discussed and now in this case the last line of receivers can be safely said to be in the far field for frequencies above

about 100 Hz. For lower frequencies, longer path length is still needed in order to get in to the far field. However, as mentioned earlier, the low frequencies also need longer window lengths for validity, so generally for these simulations analysis of results should be done with caution in the region under 100 Hz.

4.4.2 Far field

The next step was to lengthen the path lengths considerably to get properly in to the far field. The easiest way to do this is to situate the source at a distant boundary node. Then the radiated source energy is simply greater (double in the case of an ideally hard boundary) but the source characteristics are entirely equivalent to a freely radiating source. This arrangement also saves some computational resources. The source was thus situated at a boundary about 15 meters from the object and the receiver lines of 20 receivers were positioned at approximately 1 m, 2 m, ... , 6 m from the object. A real world analogue for this arrangement could be for instance a performer on a stage and audience situated at different distances from a back wall represented by the structure. Another important scenario is the way a performer hears his/her performance or how multiple performers hear each other on a stage. To mimic this scenario, the aforementioned arrangement was also used with the source positioned at 5 meters from the object.

The mean frequency responses for each line of receivers for both of the arrangements are shown in the top plots in Figure 4.12. Below the plots the differences between the mean frequency responses for the first and last line of receivers are also shown. As can be seen overall from all these responses, the low frequency notches have almost straightened out and the responses are almost identical in the region between about 500 Hz and 2 kHz. This notion is also echoed by the difference plots, especially for the case where the source is located at 15 meters where the differences between 500 Hz and 3 kHz are practically negligible. The features between these frequencies can now be reliably seen to result from the geometry of the structure. The arrangement with the source at a boundary 15 meters away from the structure, and 6 lines of 20 receivers at 1 . . . 6 meters, is the setup of choice that is utilized for the further frequency domain investigations in Section 5.
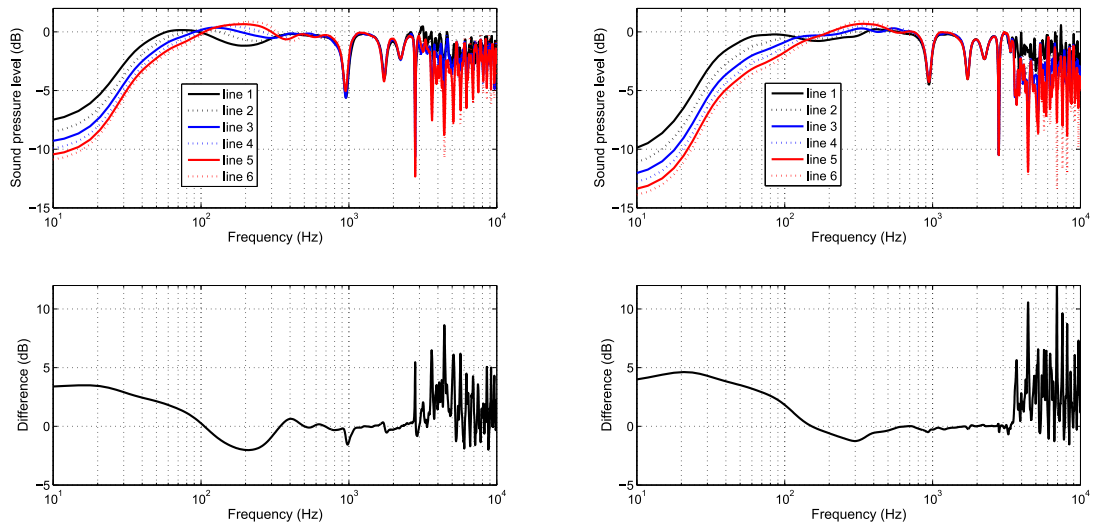
Figure 4.12: Results in the far field; source at 5 (left) and 15 (right) meters from the object. Below, the differences in the mean frequency responses for the first and last line of receivers are shown.

5   Simulations

In the following, the simulations for this thesis work are presented with the results and analyses. The simulation models are based both on practical structures and experimental structures. As precise material differentiation is not really necessary for the scope of this thesis, a global reflection coefficient of 0.95 – which is suitable for representing hard materials – is assigned for the studied structures. The aim of the simulations is to aid understanding of the reflection properties of various wall structures that feature a slatted panel and a back wall behind it, forming a cavity in between. The effects of the various features of the structure are studied by varying the dimensions of the features and observing how the responses at the receivers change.

The method of investigation is threefold: visualizations facilitate an intuitive grasp of the qualitative nature of the underlying phenomena, frequency- and time-domain analysis is used for detailed examination and diffusive properties are studied with polar response measurements. The simulations in this section are presented in the form of a logical continuum.

5.1   Continuation: slatted panel with a flat back wall

This section continues studying the structure with a slatted panel and a flat back wall, presented in Section 4.3 interlaced with the development of the simulation setup. After the establishment of a reliable setup and finding the prominent features of the response of the structure, the logical step to take is to vary the design parameters to develop further understanding. For this purpose the cavity depth of the structure was varied. 2-D FDTD visualizations were also made for normal and oblique angles of incidence in order to facilitate intuitive understanding of what occurs in the reflection.

5.1.1   Parameter: cavity depth

In addition to the already studied cavity depth of 20 cm, models with cavity depths of 30 cm, 40 cm and 50 cm were simulated. Figure 5.1 presents the mean frequency responses for all the models for different lines of receivers. A deeper cavity is seen to lower the significant notch frequencies and to uncover more of them in the high mid frequencies. Evidently, notches can be found at frequencies that are approximately multiples of each other and what is seen in the results is a comb filtering effect. It is due to the interference of reflected waves with different delays, the cause of which is the depth of the cavity. Some low frequency loss is also seen in the results, with more of the energy being lost for further lines of receivers. Also the cavity depth is seen to affect the slope of the low frequency responses by making them steeper. The cause of these effects is not known.

The application of equation (2.30) and the end correction given by equation (2.32) predict for the structure with a 20 cm cavity a resonance at 350 Hz, or 293 Hz if the meshing inaccuracies are compensated. It is clear that no trace of such a

resonance appears in the results shown in Figure 5.1. This was expected due to the fact that the features of the studied structures deviate from what is customary for distributed Helmholtz resonators. However, the literature is somewhat vague about the applicability range of the theory. The width of the openings in the structures considered here are an order of magnitude larger than usually seen in the resonator structures, being several centimeters instead of millimeters. The 50 % open area in the panel is also much greater than what is generally seen in distributed Helmholtz resonators.
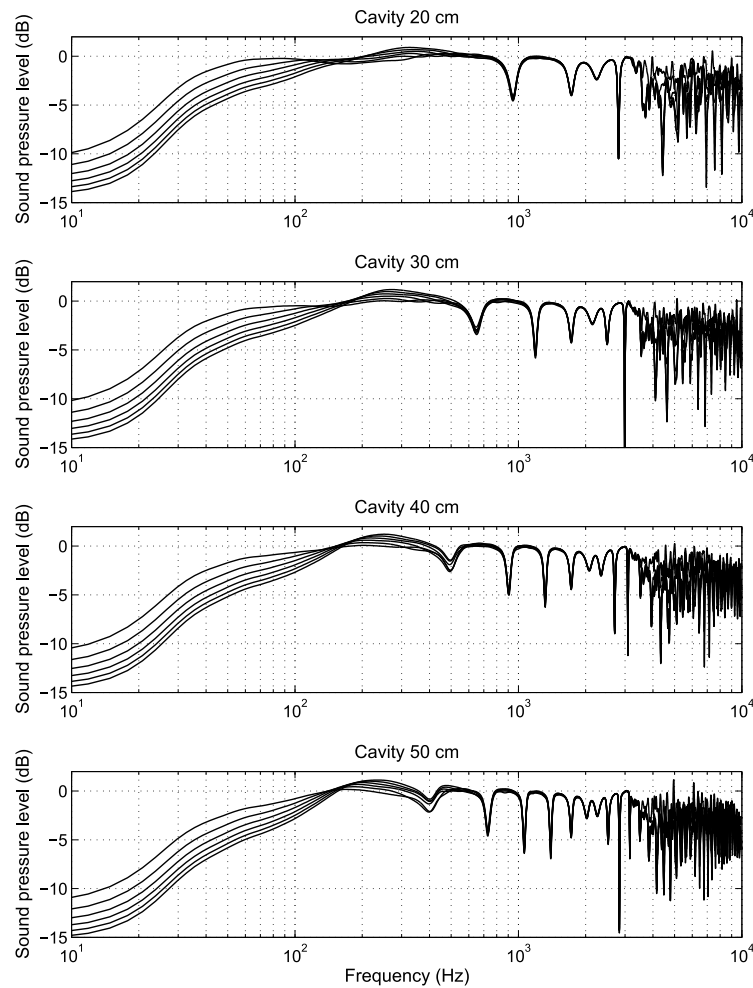
Figure 5.1: The effect of cavity depth on the mean frequency responses for different lines of receivers for the slatted panel structure with a flat back wall.

In order to acquire a sense of what occurs in the time domain, spectrogram analysis was also used. Figure 5.2 shows the reflections in the time and frequency domains for the structures with different cavity depths. The responses are taken from a single receiver at the middle of the sixth line of receivers. The dynamic range of the plot is limited in order to better highlight the arrival of individual reflections. The changing cavity depth is seen to affect the arrival time of a series of stronger

reflections. Also, the later reflections spread out more in time as the cavity depth grows, meaning that the reflections are a result of multiple successive reflections between the back wall and the panel. This shows that the structure introduces temporal spreading, the extent of which is dependent on the cavity depth.
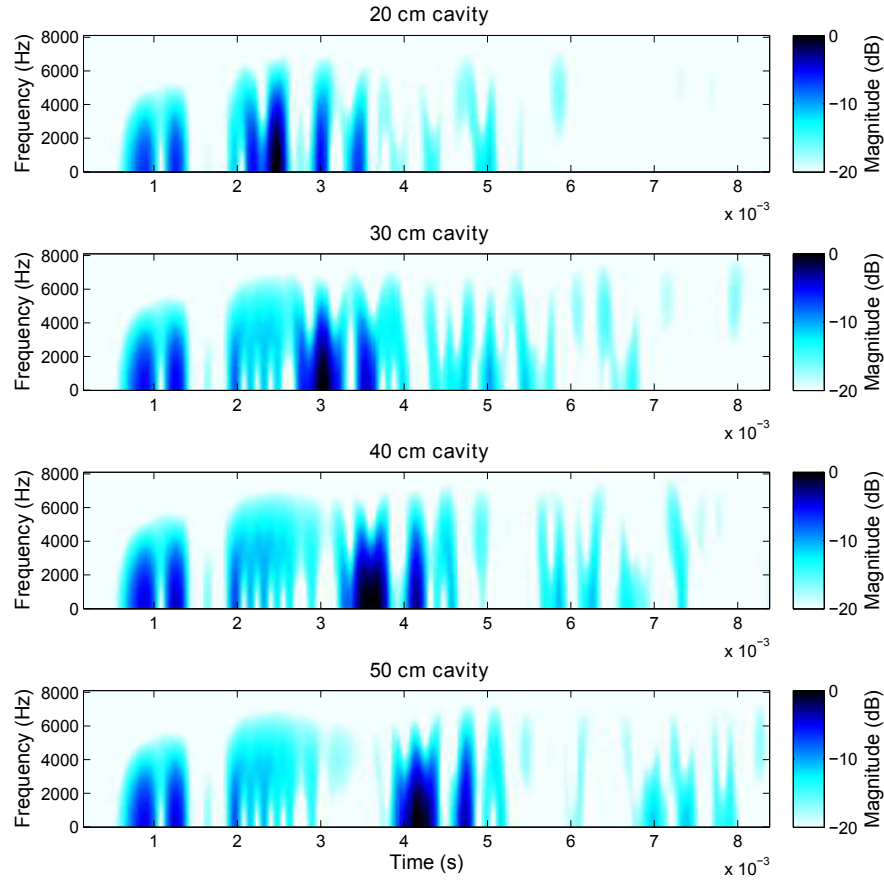

Figure 5.2: The effect of cavity depth on the time domain response of a single receiver at the middle of the sixth line of receivers for the structure with a slatted panel and a flat back wall.

5.1.2 Visualization

Figure 5.3 shows snapshots from a simulation that was specifically done for visualization purposes. The source is situated at a boundary node 5 meters away from the slatted panel. The structure is the 5 cm × 5 cm slatted panel with 50 % open area and a 20 cm back cavity. From the visualization it is readily observed how the incident wave is partly reflected by, and partly transmitted through the slatted panel. The transmitted wave is then reflected back from the cavity wall, and part of the wave passes through the panel while part of it is reflected back towards the cavity wall. In this manner, the total outgoing wave is a series of consecutive wavefronts, delayed according to the depth of the cavity and filtered by the panel. Figure 5.4

shows the color bar corresponding to this visualization that also applies to all the visualizations that are shown later on.
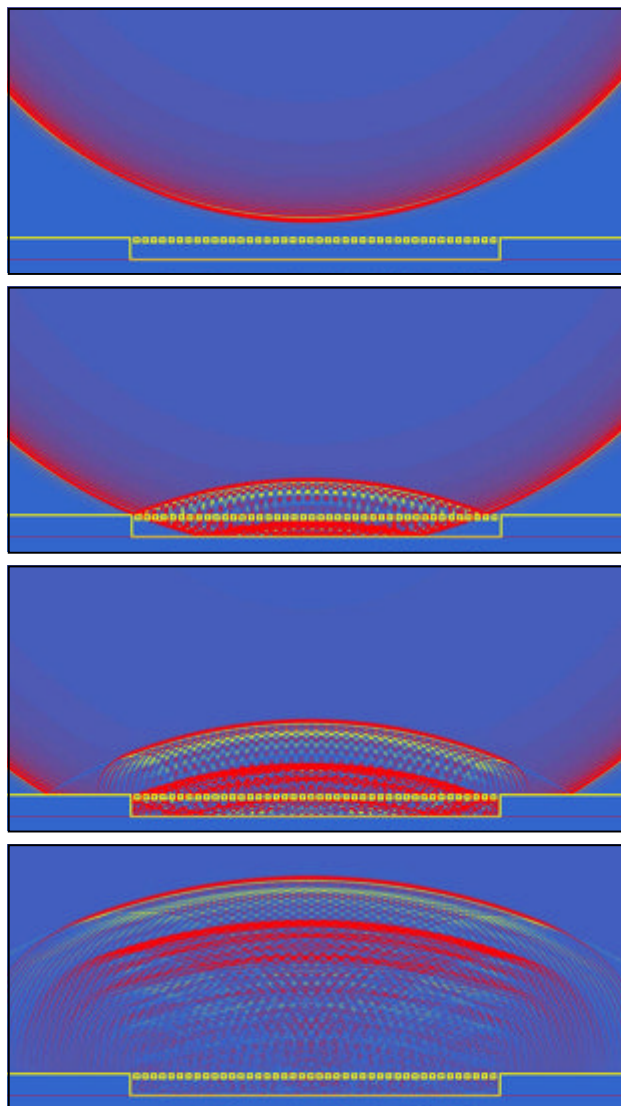

Figure 5.3: Visualization of a band-limited impulse interacting with the structure with a slatted panel and a flat back wall; source at 5 meter distance.

Figure 5.4: Color bar corresponding to the visualization(s).

Another visualization was done for a source position at 45° angle from the center of the panel in order to acquire a sense of what happens in case of oblique incidence. The visualization is shown in Figure 5.5. The result is seen to be somewhat more chaotic. It is observed that most of the sound energy is specularly reflected, but some high frequency energy is also scattered by the panel.
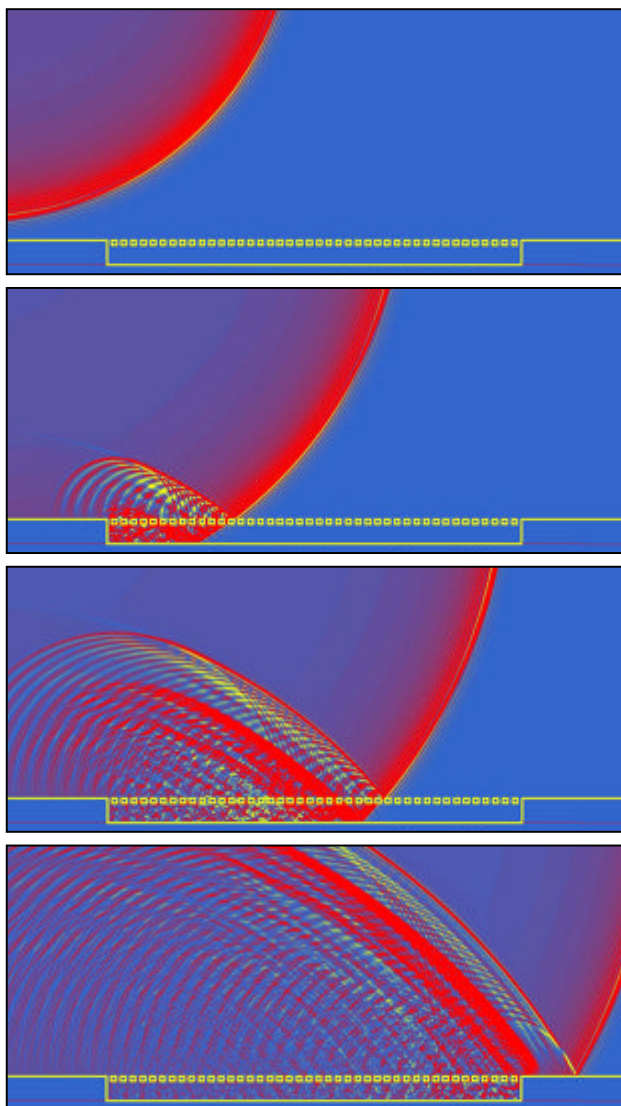
Figure 5.5: Visualization of a band-limited impulse interacting with the structure with a slatted panel and a flat back wall at oblique incidence; source at 5 meter distance and at an angle of 45° from the center of the panel.

5.2 Slatted panel

An important issue to understand is how the panel affects the incident sound. The next step was to study the panel's effect in isolation by creating a model with such a deep cavity that no sound comes back out of it in the target time window. A comparison of the time/frequency domain effects of the panel with and without the back wall is presented in Figure 5.6. The responses are from a single receiver position at the middle of the sixth line of receivers. It is easy to see from the figure that the early parts of the responses are practically identical. The early parts are therefore due to the panel only whereas the late part is caused by the back wall combined with the panel.
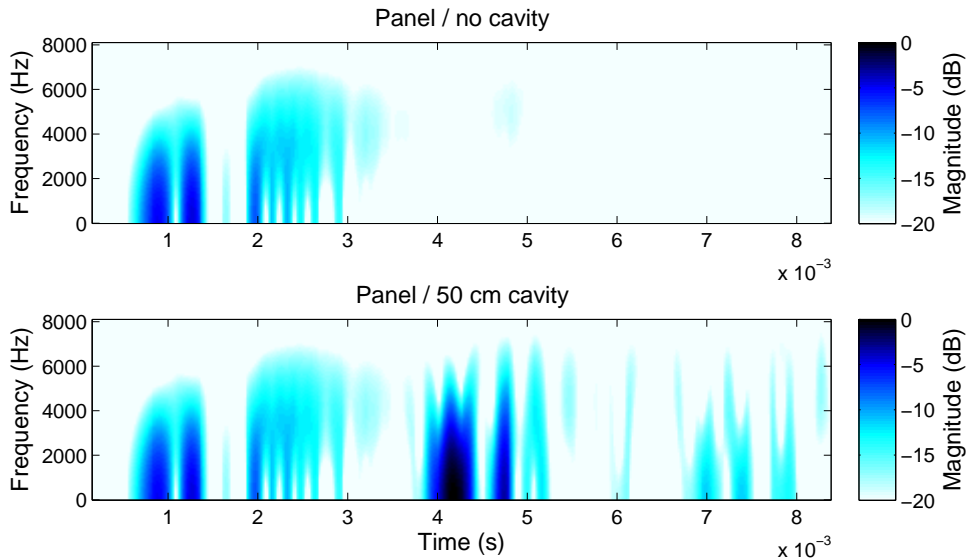
Figure 5.6: The time/frequency responses of the panel with (bottom) and without (top) the back wall, for a single receiver at the middle of the sixth line of receivers. The panel has 5 cm × 5 cm dimensions and 50 % open area in both cases.

5.2.1 Parameter: slat width

The next step was to study the panel effects by changing its features. The slat width was the first parameter to vary. Figure 5.7 shows the results for three different slat widths (keeping the thickness of the panel constant) with 50 % open area in all models. Only the mean responses for the furthest line of receivers is shown, for clarity. It was confirmed through visual scrutiny that the other receiver lines showed similar features. It can be seen that the panel acts as a high pass filter, reflecting a significant portion of the high frequencies and passing most of the low frequencies through unaffected. The wider the solid parts of the panel are, the more the structure reflects the low frequencies. The difference is subtle, due to the open area – which is kept equal throughout the models – being the primary factor that determines how much of the incident sound is reflected.

An interesting feature of the responses is the notch frequency that changes with the width of the slats. The changing depth of the notch is possibly caused by the change in the amount of slats; the width of the whole panel is equal between all the simulated models and thus the amount of repetitions in the slatted structure diminishes as the width of the slats grows.
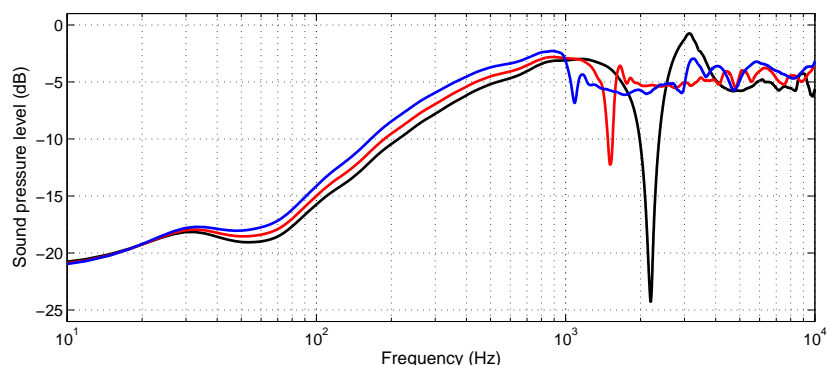

Figure 5.7: Effect of the slat width. Slat dimensions: black = 5 cm × 5 cm, red = 10 cm × 5 cm, blue = 15 cm × 5 cm.

5.2.2   Parameter: panel thickness

The next parameter to study was the thickness of the panel. Figure 5.8 shows how the average response of the sixth line of receivers changes with the slat thickness. It is clear that a thicker panel lowers the notch frequency. Also, a further notch for the 5 cm × 10 cm panel becomes visible at about double the frequency of the first. The same applies for the 5 cm × 15 cm panel that also has an additional third notch at three times the frequency of the first. The structure thus introduces comb filtering with the notches reaching down to about -15 dB below the overall level of the mid and high frequencies. The thicker panels also reflect significantly more of the low frequencies, as expected.
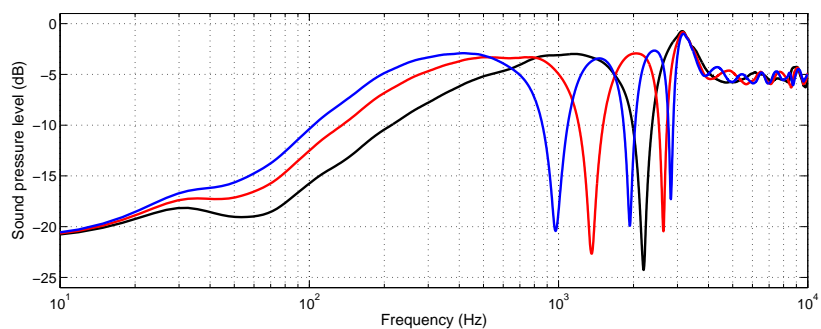

Figure 5.8: Effect of the slat thickness. Slat dimensions: black = 5 cm × 5 cm, red = 5 cm × 10 cm, blue = 5 cm × 15 cm.

5.2.3 Parameter: percentage of open area

The percentage of open area was the next object of study. The study was done for panels with 5 cm × 5 cm slats, by changing the spacing between the solid blocks. Figure 5.9 shows the results for four different porosities. It is easily seen that less porosity means that the panel reflects all frequencies better, as can be expected. A wider spacing between the solid blocks also lowers the notch frequency near 2 kHz.
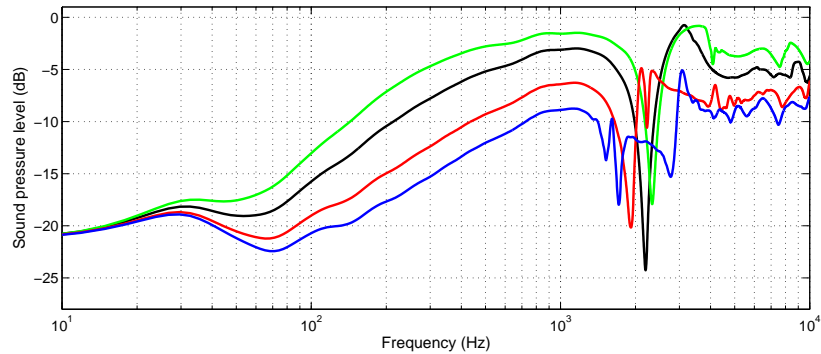

Figure 5.9: Effect of the panel porosity. Spaces: green = 3 cm, black = 5 cm, red = 10 cm, blue = 15 cm.

5.2.4 Visualization

Finally, a 2-D FDTD visualization was done to study the panel effect. Figure 5.10 shows snapshots from the visualization. As can be seen, the panel acts as a filter that reflects a portion of the incident wave back and passes the other portion through. Moreover, the passed frequencies are predominantly lower than the reflected frequencies.

5.3 Slatted panel with a convex back wall

After studying the effect of the cavity depth and the different variables of the slatted panel, the next step was to study different back wall shapes. First, a slightly convex back wall was studied where the back wall has the shape of an arc with a bulge of 10 cm. A reference model with a flat wall is also included that results in the same average cavity depth. Figure 5.11 shows the average frequency responses for the sixth receiver lines for both models. It can be seen that the structure with the convex back wall exhibits similar features in the response but the notch frequencies are shifted upwards. This shifting effect is probably due to the local depth of the structure being less and thus resulting in higher depth-dependent resonances, although the average cavity depth is equal.
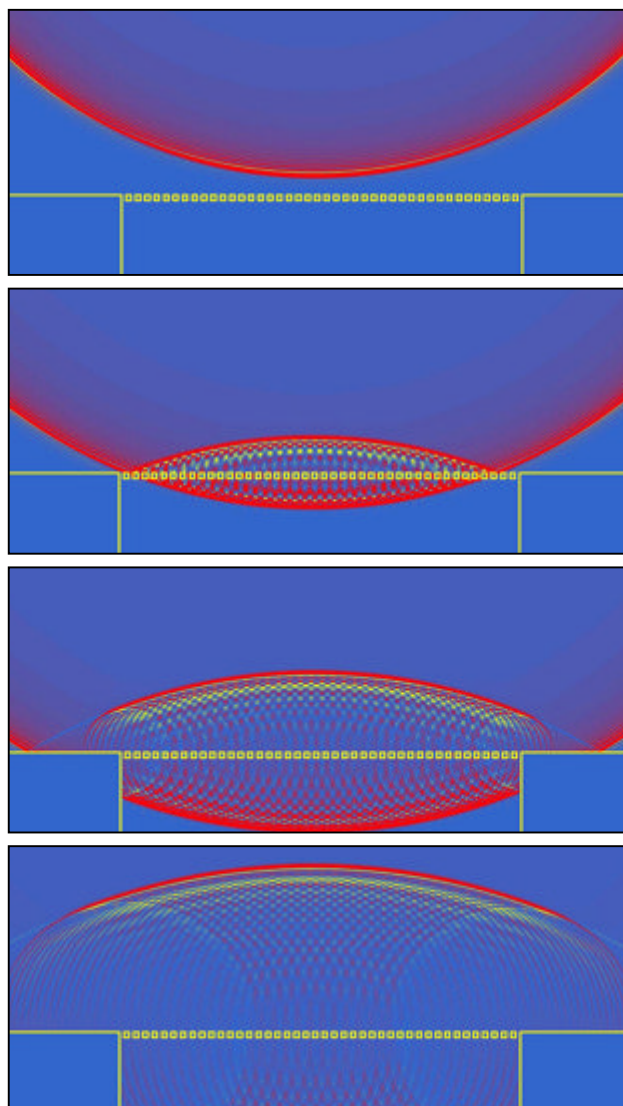
Figure 5.10: Visualization of a band-limited impulse interacting with the slatted panel; source at 5 meter distance.
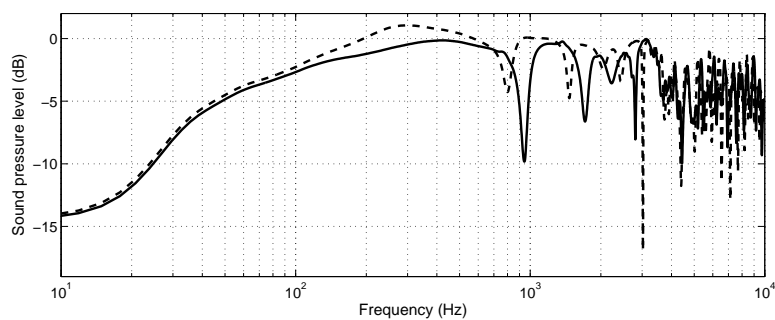

Figure 5.11: Mean frequency response for the furthest line of receivers for the slatted panel with a convex back wall (solid line) and a reference case with a slatted panel and a flat wall, resulting in equal average cavity depth (dashed line).

5.3.1 Visualization

Figure 5.12 shows a visualization of the reflection from the structure with the convex back wall. It is evident that compared to the flat wall case, the reflected wavefront is more curved. Furthermore, it is clearly seen that the delayed wavefronts are progressively more curved, which is due to the effect of the back wall curvature being applied several times through consecutive reflections between the panel and the back wall.
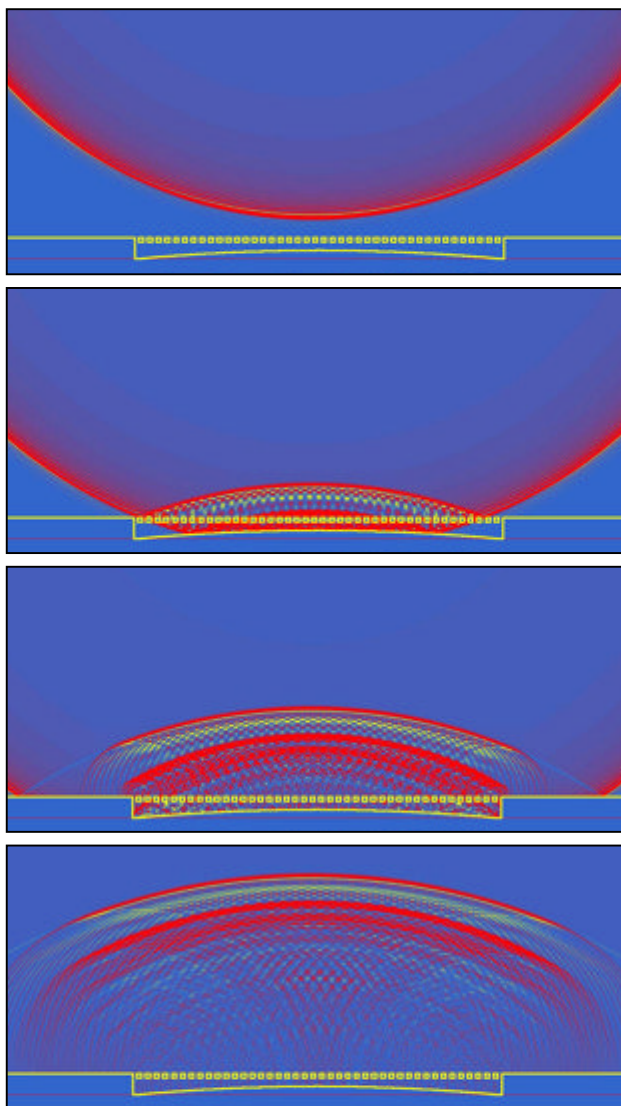

Figure 5.12: Visualization of a band-limited impulse interacting with the structure with a slatted panel and a convex back wall; source at 5 meter distance.

5.4 Slatted panel with a sawtooth corrugated back wall

The next back wall shape comes from a practical example. Figure 5.13 shows one of the walls directly behind a seating area at the Helsinki Music Centre Concert Hall
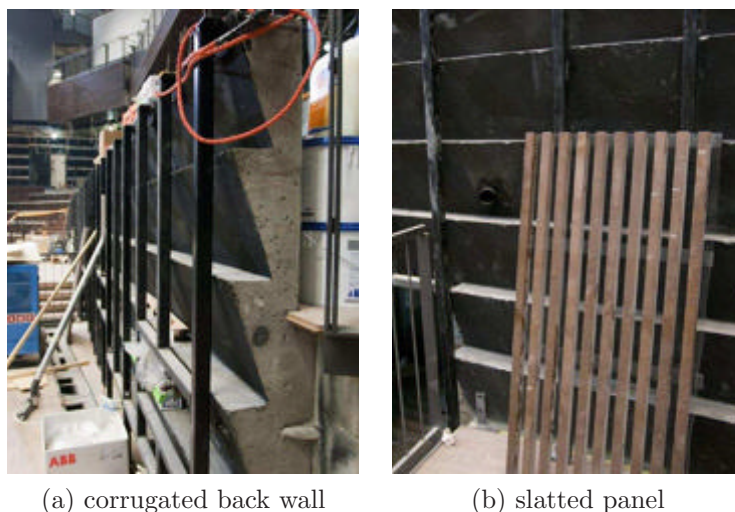
(a) corrugated back wall　　　　(b) slatted panel

Figure 5.13: An audience area back wall during the construction phase at Helsinki Music Centre Concert Hall. Photos courtesy of Jukka Pätynen.

during the construction phase. The photo on the left shows the back wall structure, a sawtooth-shaped corrugated wall made out of concrete. In front of the wall are supports made out of metal, on which wooden slatted panels are later installed. The photo on the right shows one such panel, waiting for installation. The panels are installed so that the slats are horizontal in the final structure. For the next object of study, an approximate model of this structure was made based on the photos in Figure 5.13. A 5 cm × 5 cm slatted panel was coupled with a sawtooth-shaped back wall corrugation of period length 40 cm. The amplitude of the corrugations is 15 cm, thus resulting in minimum and maximum cavity depths of 5 cm and 20 cm, respectively. In this case, the vertical response of the structure is studied as the structural symmetry is with respect to the side directions. It should be noted here that the original purpose of this structure is not known to the author of this thesis.

As mentioned in Section 2.1.6 on resonance, with Helmholtz resonant structures the volume of the cavity is the primary parameter, not the exact shape of the cavity. Thus, for reference purposes a model with a slatted panel and a flat back wall was made having the same average cavity depth as the corrugated back wall structure. Figure 5.14 presents the obtained average results for six lines of receivers for the corrugated model and the flat model. As can be seen, the overall envelope of the responses for the corrugated model is similar to the flat model, especially at low frequencies. However, for the corrugated model a very narrow notch that exceeds 10 dB in depth can be found at 700 Hz for all lines of receivers. In addition, some high frequency loss is evident between 700 Hz and 3 kHz, the greatest notch being at slightly above 2 kHz. The effect becomes more prominent as the distance from the structure grows, which suggests diffusive behaviour.
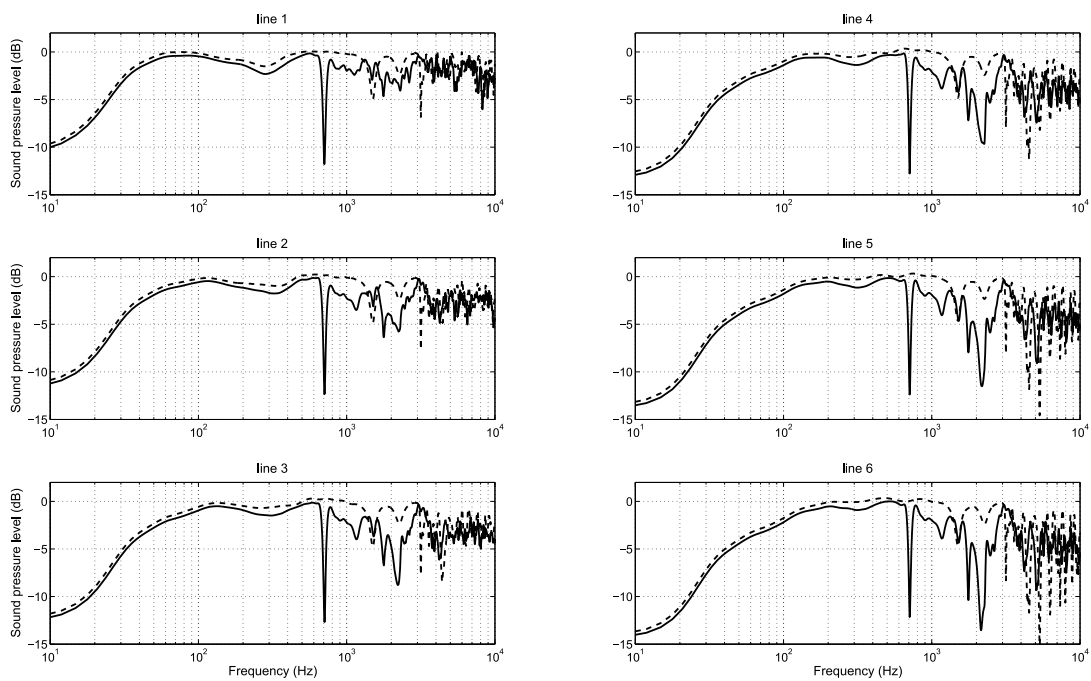
Figure 5.14: Mean frequency responses for lines of receivers for the saw corrugated model (solid line) and for the flat wall model (dashed line) with the same average cavity depth.

5.4.1 Parameter: cavity depth

To learn more about the saw corrugated structure, the cavity depth and the corrugation features were varied in order to obtain a grasp of their effects. First, the cavity depth was varied while keeping the dimensions of the back wall corrugation the same. Figure 5.15 shows the mean frequency responses for six lines of receivers for models having maximum cavity depths of 20, 30 and 40 cm. The 20 cm cavity corresponds to the previous results shown in Figure 5.14. The increasing cavity depth can be seen to lower the prominent notch frequency slightly, from 700 Hz to about 600 Hz, and to introduce an additional notch at a higher frequency than the first. Otherwise, the responses remain mostly similar.
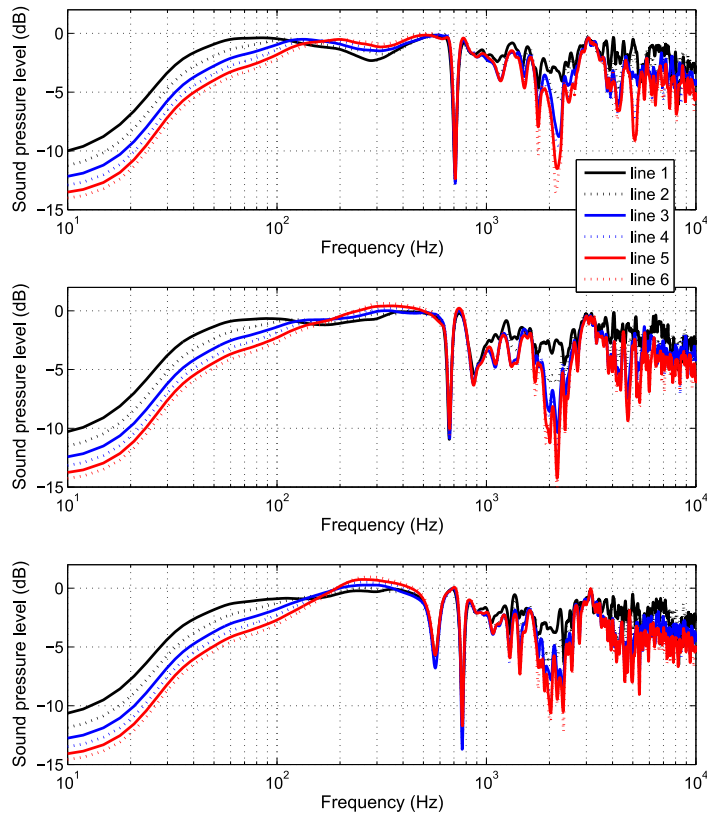

Figure 5.15: Mean frequency responses for six lines of receivers for maximum cavity depths of 20 cm (top), 30 cm (middle) and 40 cm (bottom).

5.4.2 Parameter: period length

The next feature to study was the period length of the corrugation. For this purpose, two additional models with period lengths of 30 cm and 50 cm, were built. Figure 5.16 presents the results for three different period lengths. The period length is seen to affect the notch frequency in such a way that for a larger period length the frequency is lower and vice versa. The higher frequencies seem to exhibit similar

overall curves for all period lengths while there are differences in the fine structure of the responses. The low frequencies, however, are seen to be unaffected by the period length.
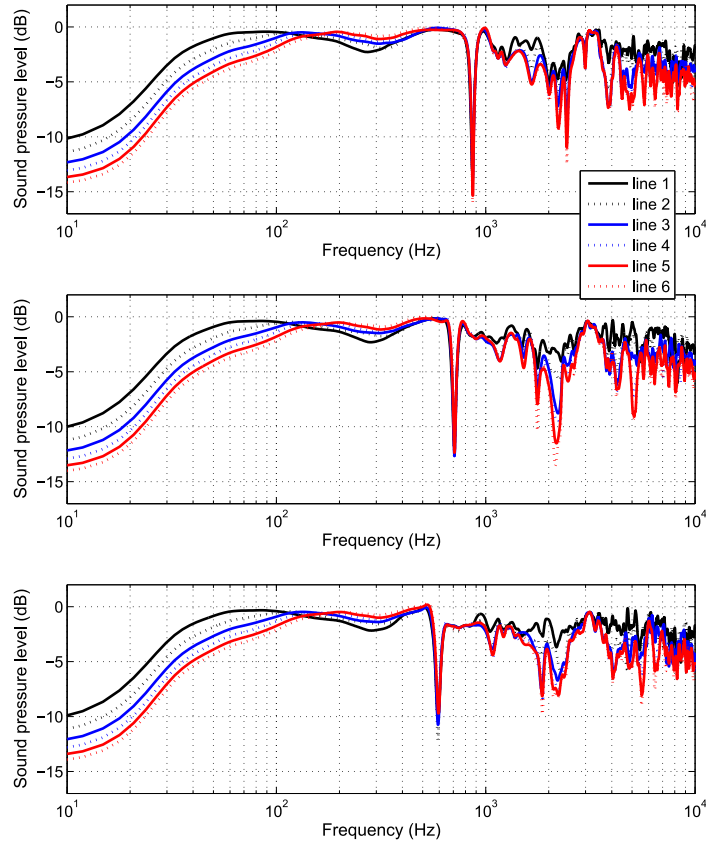

Figure 5.16: Mean frequency responses for six lines of receivers for period lengths of 30 cm (top), 40 cm (middle) and 50 cm (bottom).

5.4.3 Parameter: corrugation amplitude

The next feature to vary was the amplitude of the saw corrugations, i.e. the difference between minimum and maximum cavity depths, while retaining the average cavity depth across the simulated models. Figure 5.17 gives the results for three different amplitudes. As a reference, a model was used that had the same average cavity depth as all the varied cases. The increase in the amplitude of the corrugations can be observed to lower the notch frequency. Comparing the responses to the references shows that there is some similarity between the notch positions between the structures, which is supposedly related to the average cavity depth. Between the different models there is quite much difference in the responses between 1 kHz and 3 kHz.
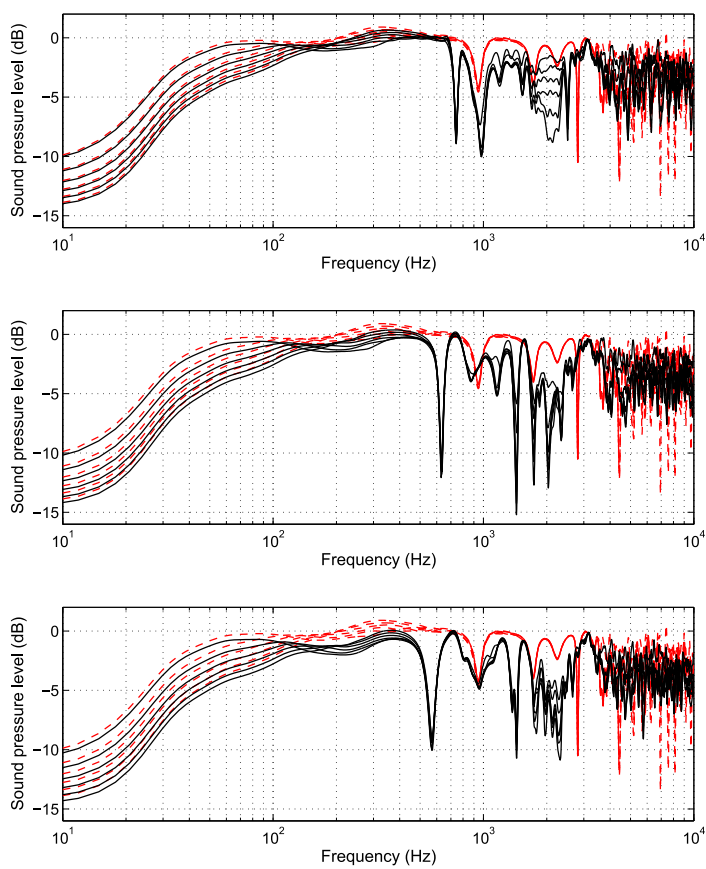
Figure 5.17: Mean frequency responses for six lines of receivers (solid black lines) for corrugation amplitudes of 10 cm (top), 20 cm (middle) and 30 cm (bottom); the reference responses (red dashed lines) are for a slatted panel structure with a flat wall at a depth of 20 cm.

5.4.4 Visualization

Figure 5.18 shows a 2-D visualization of an impulse incident on the saw corrugated structure. The effect of the cavity wall corrugation is clearly seen in that the delayed wavefronts are broken up into multiple smaller wavefronts that distribute some of the energy to the both of the side directions, away from the specular reflection direction. The structure is therefore seen to exhibit definite diffusive properties. Furthermore, slightly more of the energy is directed to the left side because of the orientation of the back wall corrugation.
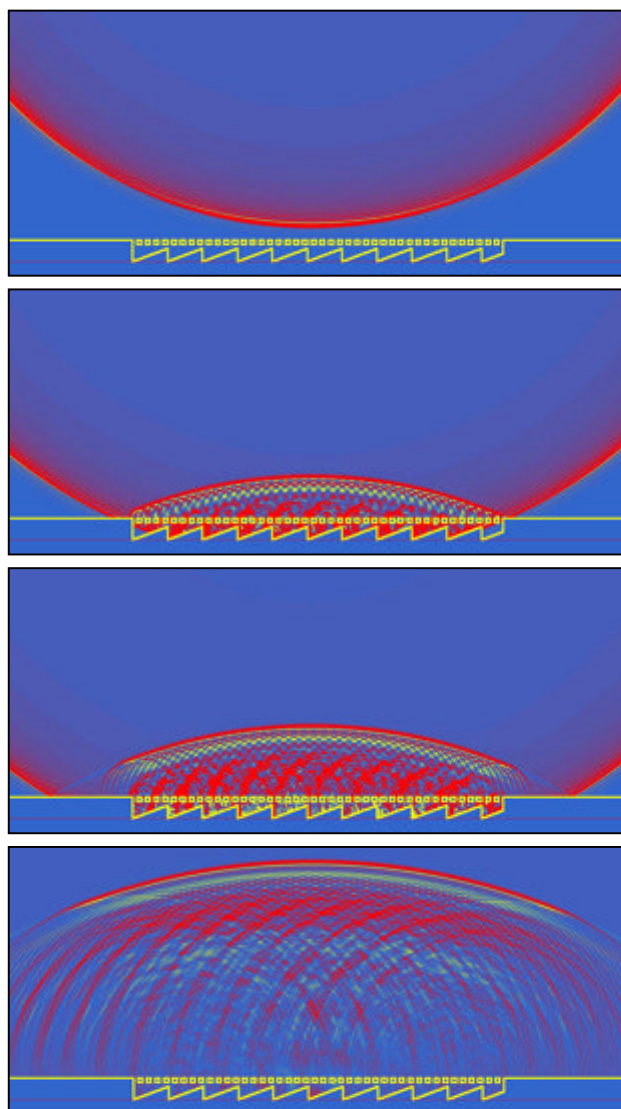

Figure 5.18: Visualization of a band-limited impulse interacting with the structure with a slatted panel and a corrugated back wall; source at 5 meter distance.

5.4.5 Measurement of diffusing properties

The logical next step was to study the diffusive properties of the slatted panel/saw corrugated back wall structure in more detail. To this end, the technique for polar response measurements – as presented in Section 2.2.4 – was utilized. The measurement setup was as follows. 37 receivers were situated on a semicircle, 5° apart and 5 meters away from the center of the target structure. 19 source positions likewise mapping out a semicircle, 10° apart and 10 meters away from the center of the structure, were used. The width of the structure was chosen to be 2.1 meters, which is somewhat large compared to the measurement setup geometry but still conforms to the requirement of at least 80 % of the receivers being outside the specular zone for each source position.

The requirement for diffusion measurements is that for periodic structures at least four full periods should be present in order for the results to be representative of the full structure. The width of the structure here accommodates five full periods of 40 cm length saw corrugations and enclosing edges and thus fulfills the criterion. The structure is similar to the one whose frequency responses for several lines of receivers were shown in Figure 5.14 and that was modelled after the structure shown in Figure 5.13. The only difference between the two studied models is the width of the whole structure, and thus the number of corrugation periods and slats. The difference here is unavoidable due to limitations imposed by the requirements of the polar response measurement method. The former structure would simply require too big of a mesh for simulation.

In accordance to the measurement technique specifications, the simulations were also run for a reference flat panel of equal dimensions, for reference purposes and normalization of the calculated diffusion coefficients. Additionally, the simulations were run within an empty space in order to obtain only the direct sound at receivers, for subtraction purposes. In total, the 19 source positions were separately simulated for all the three models – the investigated structure, the reference flat panel, and empty space – giving a total of 57 simulations. The results were filtered to get rid of aliasing effects and the direct sound was subtracted from the test subject and reference panel responses. The results for the polar responses of one studied structure were then contained in $19 \times 37 = 703$ separate impulse responses.

The starting points for the individual reflection responses were algorithmically detected in order to allow for automatic and careful placement of windows. The reference flat surface responses (direct sound subtracted) were used to find the start points for individual reflection responses and the same start points were then used for extracting both the reference and sample responses. A vector of ones was concatenated with a half Hann window to form the windowing function that smooths the signals gradually to zero in order to avoid truncation problems. The same window length was used for all the responses and the length was chosen so as to allow the exclusion of the boundary reflections at each receiver point.

After the isolation and windowing of responses, the next step was to construct from each set of 37 responses the polar responses for 1/3 octave bands for each angle of incidence. The energy of each individual receiver response was summed up over

1/3 octave bands and the 37 responses for one source position were then combined to form the polar responses. This procedure was done for all angles of incidence for both the saw corrugated structure and the flat panel. Figure 5.19 shows a subset of the polar responses for both the saw corrugated structure and the reference flat panel. It is evident that in the 250 Hz band the corrugated structure does not exhibit diffusive properties but in the 630 Hz band a clear diffusion effect is already found at oblique angles. This effect is likely due to the corrugated back wall because it is in this frequency range that the back wall corrugation dimensions are comparable to the wavelength (see Section 2.1.4 on scattering). The higher frequency bands show more scattering effects and also at normal incidence, which suggests that the panel plays a significant role in the scattering effects at these frequencies.
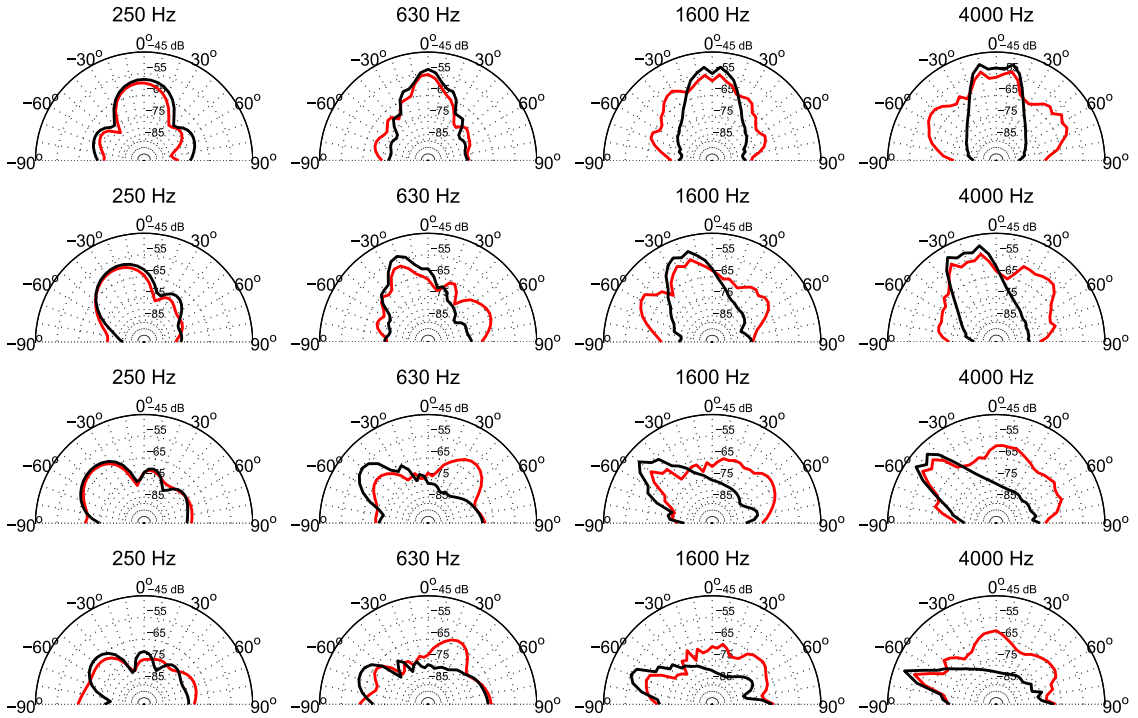

Figure 5.19: Polar responses for a subset of 1/3 octave bands for 0° (first row), 20° (second row), 50° (third row) and 70° (bottom row) incidence angles; black lines = reference flat panel, red lines = slatted panel with saw corrugated back wall.

The autocorrelation diffusion coefficient values for the 1/3 octave bands for each angle of incidence were calculated with equation (2.47). The average diffusion coefficients for both the studied structure and the reference panel were then obtained by taking the arithmetic mean over all angles of incidence. The normalized diffusion coefficient for the studied structure was obtained through application of the coefficient values to equation (2.48) and rectifying any negative values to 0, as instructed. The diffusion coefficient values for the reference flat panel as well as both the unnormalized and normalized diffusion coefficient values for the saw corrugated structure are shown in Figure 5.20. The maximum of the coefficient is found at 2 kHz, which corresponds to the notch found in the results presented in Figure 5.14. The notch is

more prominent for further receiver distances which makes sense because the structure is particularly diffusive at these frequencies. The energy at these frequencies passes by the receivers near the structure because the redirected path is still within their reach but does not pass by the more distant receiver points.
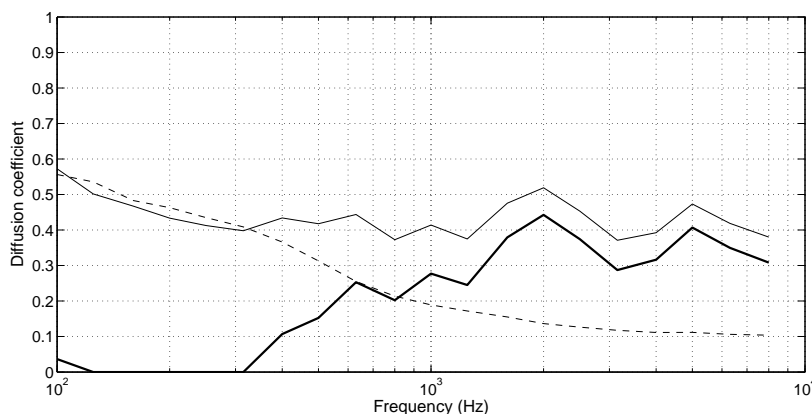

Figure 5.20: The diffusion coefficient values for the reference flat panel (dashed line) and the saw corrugated slatted panel structure (solid lines). The thick line denotes the normalized diffusion coefficient value.

In order to get further perspective into the results, the polar response measurements were also conducted for the slatted panel structure with a flat back wall that has equal average cavity depth with the saw corrugated structure. Figure 5.21 shows a subset of the polar responses for this structure from the same 1/3 octave bands as in Figure 5.19. Compared to the results in Figure 5.19, the flat wall structure is clearly less diffusive at the 630 Hz and 1600 Hz bands, while in the 4 kHz band the amount of diffusion is prominent although still less than for the saw corrugated structure.

Normalized and unnormalized diffusion coefficient values for the flat wall structure are given in Figure 5.22. Comparing this to the diffusion coefficients in Figure 5.20 allows the observation to be made that the structure with the saw corrugation shows considerably more diffusive behaviour between approximately 600 Hz and 5 kHz than the structure with the flat back wall. However, the flat wall structure shows more diffusion at and below about 500 Hz. It is below these frequencies that the wavelength becomes comparable to the cavity side length, which is 2 meters. Therefore it may be a source of resonances at this frequency range. It may be due to these resonances being less inhibited because of the flat back wall that the full structure shows more diffusion at these frequencies compared to the saw corrugated structure.
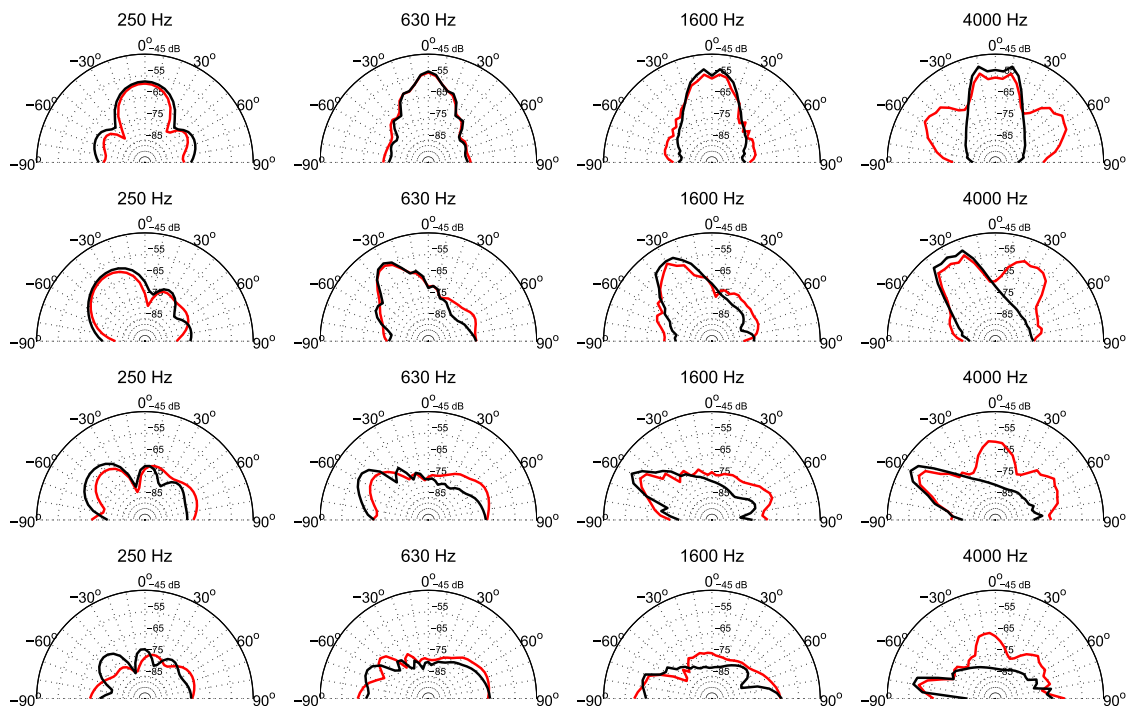
Figure 5.21: Polar responses for a subset of 1/3 octave bands for 0° (first row), 20° (second row), 50° (third row) and 70° (bottom row) incidence angles; black lines = reference flat panel, red lines = slatted panel with flat back wall.

Figure 5.22: The diffusion coefficient values for the reference flat panel (dashed line) and the slatted panel structure with a flat back wall (solid lines). The thick line denotes the normalized diffusion coefficient value.

6 Conclusions

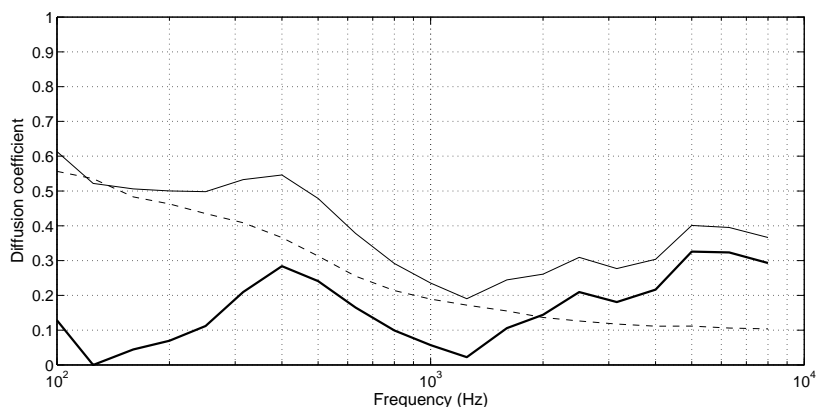The sound reflection properties of layered wall structures were studied using the 2-D standard rectilinear (SRL) finite-difference time-domain (FDTD) method for simulating acoustic wave propagation in an isotropic medium. FDTD belongs to the branch of wave-based acoustic modelling methods and it is successful in modeling accurately the diffraction and interference effects that are crucial for proper representation of the wave nature of sound, especially at low frequencies.

The relevant background in wave acoustics was briefly reviewed alongside acoustic measurement methods, of which the method for polar response measurements was later utilized for evaluation of diffusive properties of structures. Various geometric and wave-based acoustic modelling methods were also briefly discussed. The SRL FDTD method used in this thesis was separately handled with the discussion of the specifics of the 3-D version. Discussion on the simulation setup followed and a few introductory simulations explored the 2-D and 3-D SRL FDTD methods. A comparison of the results from the 2-D and 3-D methods showed that the results can be qualitatively equivalent when the structure has one axis of symmetry. The 2-D method was therefore deemed a more suitable alternative for this thesis work.

The studied wall structures consist of a front panel with slats coupled with a back wall, forming a cavity in between. Structures resembling these are generally known in the literature as *distributed Helmholtz resonators* or *resonant absorbers*. However, the structures studied in this thesis have a different parameter range and include no loss mechanism (i.e. absorption) and therefore can not be considered effectively to be such structures. A multitude of models were made with varied structural features to study their effects on the reflection responses. For the simulations, 2-D slices of the models were meshed.

The slatted panel by itself was found to be frequency-selective in reflecting and transmitting sound. Generally, the slatted panel tends to transmit most of the low frequencies through while reflecting most of the high frequencies. Therefore the slatted panel acts as a kind of filter for the incident sound. The panel also introduces a notch in the frequency response. A widening of the slat width was seen to slightly enhance the low frequency reflectivity while also lowering the notch frequency. Thickening of the panel lowers the notch frequency and enhances the low frequency reflectivity considerably. Additional notches were also seen to be uncovered at multiples of the first frequency, revealing a comb filtering effect of the structure. It was also found that the less open area in the panel, the better the panel reflects sound, as was expected.

Coupling the panel with a flat back wall created a resonant system where the panel acts as a filter, and the cavity acts as a delay line. The overall reflected sound was seen to consist of multiple successive wavefronts, generated by the combination of delays imposed by the cavity depth, and the accumulated filtering by multiple interactions with the panel. In the frequency domain, the effect of the structure was seen as a comb filter effect, due to the interference between the differently delayed wavefronts. Moreover, the structure introduces frequency-dependent temporal spreading, as was seen from the spectrogram analysis and the visualization.

A deeper cavity depth introduces a greater degree of temporal spreading because of the greater time differences between the successive reflections. Through visualization it was seen that changing the back wall shape to convex influences the successive wavefronts by making them progressively more bendy.

The panel coupled with the saw corrugated back wall, as found in the Concert Hall in Helsinki Music Centre behind the audience area, was seen to generate a very selective notch at mid frequencies. The frequency of this notch was seen to be influenced by all the parameters related to the back wall shape; the overall cavity depth, the period length and the corrugation amplitude. Furthermore, the structure was found to exhibit clear diffusive properties at frequencies above about 500 Hz. Measurement of polar responses from the structure revealed a maximum value for the normalized diffusion coefficient of almost 0.45 at the 1/3 octave band centered on 2 kHz. This maximum value coincides with the frequency response measurements that show a clearly identifiable notch at the same frequency for the further lines of receivers. This clearly shows that the notch results from the diffusive properties of the structure. On the other hand, the slatted panel coupled with the flat back wall does not exhibit appreciable diffusion at the same frequency range. Therefore the saw corrugated back wall can be said to be the influence behind majority of the diffusion in the mid to high frequency range.

References

[1] H. Kuttruff. *Room Acoustics*. Taylor & Francis, fifth edition, 2009.

[2] N. Xiang and J. Blauert. Binaural scale modelling for auralisation and prediction of acoustics in auditoria. *J. Appl. Acoust.*, 38:267–290, 1993.

[3] http://sketchup.google.com/. last accessed: 24/02/2012.

[4] P. M. Morse and K. U. Ingard. *Theoretical Acoustics*. McGraw-Hill, first edition, 1968.

[5] T. J. Cox, B.-I. L. Dalenback, P. D'Antonio, J. J. Embrechts, J. Y. Jeon, E. Mommertz, and M. Vorländer. A tutorial on scattering and diffusion coefficients for room acoustic surfaces. *Acta Acustica United With Acustica*, 92:1–15, 2006.

[6] M. Vorländer. International round robin on room acoustical computer simulations. In *Proc. of the 15th International Congress on Acoustics*, pages 689–692, Trondheim, Norway, June 1995.

[7] T. J. Cox and P. D'Antonio. *Acoustic Absorbers and Diffusers: Theory, design and application*. Taylor & Francis, second edition, 2009.

[8] T. Lokki, J. Pätynen, S. Tervo, S. Siltanen, and L. Savioja. Engaging concert hall acoustics is made up of temporal envelope preserving reflections. *J. Acoust. Soc. Am.*, 129:EL223–EL228, 2011.

[9] M. Long. *Architectural Acoustics*. Elsevier, first edition, 2006.

[10] T. E. Vigran. *Building Acoustics*. Taylor & Francis, first edition, 2008.

[11] T. J. Schultz. *Acoustical Uses For Perforated Metals: Principles and Applications*. Industrial Perforators Association, Inc., 1986.

[12] M. Vorländer and E. Mommertz. Definition and measurement of random-incidence scattering coefficients. *Applied Acoustics*, 60:187–199, 2000.

[13] AES-4id-2001. AES information document for room acoustics and sound reinforcement systems – characterization and measurement of surface scattering uniformity. *J. Audio Eng. Soc.*, 49:149–165, 2001.

[14] M. Kleiner, B.-I. Dalenbäck, and P. Svensson. Auralization – an overview. *J. Audio Eng. Soc.*, 41:861–875, 1993.

[15] U. P. Svensson and U. R. Kristiansen. Computational modelling and simulation of acoustic spaces. In *AES 22nd International Conference on Virtual, Synthetic and Entertainment Audio*, pages 1–20, 2002.

[16] D. Murphy, M. Beeson, S. Shelley, A. Moore, and A. Southern. Hybrid room impulse response synthesis in digital waveguide mesh based room acoustics simulation. In *Proc. of the 11th Int. Conference on Digital Audio Effecs (DAFx-08)*, Espoo, Finland, September 2008.

[17] S. Siltanen, T. Lokki, and L. Savioja. Rays or waves? Understanding the strengths and weaknesses of computational room acoustics modeling techniques. In *Proc. of ISRA*, Melbourne, Australia, August 2010.

[18] A. Southern, S. Siltanen, and L. Savioja. Spatial room impulse responses with a hybrid modelling method. In *AES 130th Convention*, London, UK, May 2011. AES Preprint 8385.

[19] S. Siltanen, T. Lokki, S. Kiminki, and L. Savioja. The room acoustic rendering equation. *J. Acoust. Soc. Am.*, 122:1624–1635, 2007.

[20] J. B. Allen and D. A. Berkley. Image method for efficiently simulating small-room acoustics. *J. Acoust. Soc. Am.*, 65:943–950, 1979.

[21] J. Borish. Extension of the image model to arbitrary polyhedra. *J. Acoust. Soc. Am.*, 75:1827–1836, 1984.

[22] U. P. Svensson, R. I. Fred, and J. Vanderkooy. An analytic secondary source model of edge diffraction impulse responses. *J. Acoust. Soc. Am.*, 106:2331–2344, 1999.

[23] A. Krokstad, S. Strøm, and S. Sørsdal. Calculating the acoustical room response by the use of a ray tracing technique. *J. Sound Vib.*, 8:118–125, 1968.

[24] E.-M. Nosal, M. Hodgson, and I. Ashdown. Improved algorithms and methods for room sound-field prediction by acoustical radiosity in arbitrary polyhedral rooms. *J. Acoust. Soc. Am.*, 116:970–980, 2004.

[25] S. Siltanen, T. Lokki, and L. Savioja. Room acoustics modeling with acoustic radiance transfer. In *Proc. of ISRA*, Melbourne, Australia, August 2010.

[26] D. Botteldooren. Finite-difference time-domain simulation of low-frequency room acoustic problems. *J. Acoust. Soc. Am.*, 98:3302–3308, 1995.

[27] L. Savioja, T. Rinne, and T. Takala. Simulation of room acoustics with a 3-D finite difference mesh. In *Proc. Int. Computer Music Conf.*, pages 463–466, Aarhus, Denmark, September 1994.

[28] D. Murphy, A. Kelloniemi, J. Mullen, and S. Shelley. Acoustic modeling using the digital waveguide mesh. *IEEE Signal Processing Magazine*, 24:55–66, 2007.

[29] K. Kowalczyk and M. van Walstijn. Room acoustics simulation using 3-D compact explicit FDTD schemes. *IEEE Trans. Audio, Speech, Lang. Processing*, 19:34–46, 2011.

[30] J. R. Wright. An exact model of acoustic radiation in enclosed spaces. *J. Audio Eng. Soc.*, 43:813–820, 1995.

[31] N. Raghuvanshi, R. Narain, and M. C. Lin. Efficient and accurate sound propagation using adaptive rectangular decomposition. *IEEE Transactions on Visualization and Computer Graphics*, 15:789–801, 2009.

[32] R. Mehra, N. Raghuvanshi, L. Savioja, M. C. Lin, and D. Manocha. An efficient GPU-based time domain solver for the acoustic wave equation. *Applied Acoustics*, 73:83–94, 2012.

[33] K. S. Yee. Numerical solution of initial boundary value problems involving Maxwell's equations in isotropic media. *IEEE Transactions on Antennas and Propagation*, 14:302–307, 1966.

[34] S. Bilbao. Time domain simulation of brass instruments. In *Forum Acusticum*, Aalborg, Denmark, June 2011.

[35] S. Bilbao. Modelling of brass instrument valves. In *Proc. of the 14th Int. Conference on Digital Audio Effects (DAFx-11)*, pages 337–343, Paris, France, September 2011.

[36] J. Redondo, R. Picó, B Roig, and M. R. Avis. Time domain simulation of sound diffusers using finite-difference schemes. *Acta Acustica United with Acustica*, 93:611–622, 2007.

[37] J. Redondo, R. Picó, M. R. Avis, and T. J. Cox. Prediction of the random-incidence scattering coefficient using a FDTD scheme. *Acta Acustica United with Acustica*, 95:1040–1047, 2009.

[38] J. LoVetri, D. Mardare, and G. Soulodre. Modeling of the seat dip effect using the finite-difference time-domain method. *J. Acoust. Soc. Am.*, 100:2204–2212, 1996.

[39] T. Lokki, A. Southern, and L. Savioja. Studies on seat dip effect with 3D FDTD modeling. In *Forum Acusticum*, pages 1517–1522, Aalborg, Denmark, June 2011.

[40] T. Lokki, A. Southern, S. Siltanen, and L. Savioja. Studies of Epidaurus with a hybrid room acoustics modelling method. In *The Acoustics of Ancient Theatres Conference*, Patras, Greece, September 2011.

[41] S. Sakamoto, T. Seimiya, and H. Tachibana. Visualization of sound reflection and diffraction using finite difference time domain method. *Acoust. Sci. & Tech.*, 23:34–39, 2002.

[42] L. Savioja. Real-time 3D finite-difference time-domain simulation of low- and mid-frequency room acoustics. In *Proc. of the 13th Int. Conference on Digital Audio Effects (DAFx-10)*, Graz, Austria, September 2010.

[43] X. Yuan, D. Borup, J. Wiskin, M. Berggren, R. Eidens, and S. Johnson. Formulation and validation of Berenger's PML absorbing boundary for the FDTD simulation of acoustic scattering. *IEEE Trans. on Ultrasonics, Ferroelectrics, and Freq. Control*, 44:816–822, 1997.

[44] E. Kreyszig. *Advanced Engineering Mathematics*. John Wiley & Sons, eighth edition, 1999.

[45] E. Mommertz. Angle-dependent in-situ measurements of reflection coefficients using a subtraction technique. *Applied Acoustics*, 46:251–263, 1995.

[46] K. Kowalczyk. *Boundary and medium modelling using compact finite difference schemes in simulations of room acoustics for audio and architectural design applications*. PhD thesis, School of Electronics, Electrical Engineering and Computer Science, Queen's University Belfast, November 2008.

[47] C. Spa, J. Escolano, A. Garriga, and T. Mateos. Compensation of the afterglow phenomenon in 2-D discrete-time simulations. *IEEE Signal Processing Letters*, 17:758–761, 2010.

[48] S. Laine, S. Siltanen, T. Lokki, and L. Savioja. Accelerated beam tracing algorithm. *Applied Acoustics*, 70:172–181, 2009.